Additively manufactured biodegradable porous zinc

Li, Yageng; Pavanram, P.; Zhou, Jie; Lietaert, K.; Taheri, P.; Li, W.; San, H.; Leeflang, M. A.; Mol, J. M.C.; Jahr, H.

DOI
10.1016/j.actbio.2019.10.034

Publication date
2020

Document Version
Final published version

Published in
Acta Biomaterialia

Citation (APA)
Li, Y., Pavanram, P., Zhou, J., Lietaert, K., Taheri, P., Li, W., San, H., Leeflang, M. A., Mol, J. M. C., Jahr, H., & Zadpoor, A. A. (2020). Additively manufactured biodegradable porous zinc. *Acta Biomaterialia*, *101*, 609-623. https://doi.org/10.1016/j.actbio.2019.10.034

Acta Biomaterialia 101 (2020) 609–623

Contents lists available at ScienceDirect

Acta Biomaterialia

journal homepage: www.elsevier.com/locate/actbio

Full length article

Additively manufactured biodegradable porous zinc

Y. Li[a,*], P. Pavanram[b], J. Zhou[a], K. Lietaert[c,d], P. Taheri[e], W. Li[e], H. San[a,f], M.A. Leeflang[a], J.M.C. Mol[e], H. Jahr[b,g,1], A.A. Zadpoor[a,1]

[a] Department of Biomechanical Engineering, Delft University of Technology, Delft 2628 CD, the Netherlands
[b] Department of Anatomy and Cell Biology, University Hospital RWTH Aachen, Aachen 52074, Germany
[c] 3D Systems - LayerWise NV, Grauwmeer 14, Leuven 3001, Belgium
[d] Department of Materials Engineering, KU Leuven, Kasteelpark Arenberg 44, Leuven3001, Belgium
[e] Department of Materials Science and Engineering, Delft University of Technology, Delft2628 CD, the Netherlands
[f] School of Materials Science and Engineering, Harbin Institute of Technology, Harbin 150001, China
[g] Department of Orthopedic Surgery, Maastricht UMC+, Maastricht6202 AZ, the Netherlands

ARTICLE INFO

Article history:
Received 12 August 2019
Revised 16 October 2019
Accepted 24 October 2019
Available online 28 October 2019

Keywords:
Additive manufacturing
Zinc
scaffold
Biodegradation
Mechanical property
Biocompatibility

ABSTRACT

Additively manufacturing (AM) opens up the possibility for biodegradable metals to possess uniquely combined characteristics that are desired for bone substitution, including bone-mimicking mechanical properties, topologically ordered porous structure, pore interconnectivity and biodegradability. Zinc is considered to be one of the promising biomaterials with respect to biodegradation rate and biocompatibility. However, no information regarding the biodegradability and biocompatibility of topologically ordered AM porous zinc is yet available. Here, we applied powder bed fusion to fabricate porous zinc with a topologically ordered diamond structure. An integrative study was conducted on the static and dynamic biodegradation behavior (*in vitro*, up to 4 weeks), evolution of mechanical properties with increasing immersion time, electrochemical performance, and biocompatibility of the AM porous zinc. The specimens lost 7.8% of their weight after 4 weeks of dynamic immersion in a revised simulated body fluid. The mechanisms of biodegradation were site-dependent and differed from the top of the specimens to the bottom. During the whole *in vitro* immersion time of 4 weeks, the elastic modulus values of the AM porous zinc ($E = 700–1000$ MPa) even increased and remained within the scope of those of cancellous bone. Indirect cytotoxicity revealed good cellular activity up to 72 h according to ISO 10,993–5 and -12. Live-dead staining confirmed good viability of MG-63 cells cultured on the surface of the AM porous zinc. These important findings could open up unprecedented opportunities for the development of multifunctional bone substituting materials that will enable reconstruction and regeneration of critical-size load-bearing bone defects.

Statement of significance

No information regarding the biodegradability and biocompatibility of topologically ordered AM porous zinc is available. We applied selective laser melting to fabricate topologically ordered porous zinc and conducted a comprehensive study on the biodegradation behavior, electrochemical performance, time-dependent mechanical properties, and biocompatibility of the scaffolds. The specimens lost 7.8% of their weight after4 weeks dynamic biodegradation while their mechanical properties surprisingly increased after 4 weeks. Indirect cytotoxicity revealed good cellular activity up to 72 h. Intimate contact between MG-63 cells and the scaffolds was also observed. These important findings could open up unprecedented opportunities for the development of multifunctional bone substituting materials that mimic bone properties and enable full regeneration of critical-size load-bearing bony defects.

1. Introduction

The recent advent of additive manufacturing (AM) techniques has caused a breakthrough in the manufacturing of porous metallic bone substitutes for bone regeneration [1–3]. AM can precisely

* Corresponding author.
E-mail address: y.li-7@tudelft.nl (Y. Li).
[1] Authors contributed equally to the study.

https://doi.org/10.1016/j.actbio.2019.10.034
1742-7061/

control and customize the geometry of porous biomaterials to match the mechanical properties of the human bone [4,5], while a fully interconnected porous structure, a large bio-functionalized surface area [6], and an appropriate range of permeability values facilitate cell proliferation and differentiation [7]. Up till now, a number of metallic AM porous biomaterials, such as stainless steel [8], titanium alloys [9,10], tantalum [11], and cobalt-chromium alloys [12], have been studied. However, all these non-biodegradable implants cause chronic local inflammation and physical irritation and, thus, may necessitate a second surgery [13]. Furthermore, the risk of recrudescent and hardly curable implant-related infections that often incur from non-biodegradable implants is permanently present [14]. AM biodegradable porous metals with proper biodegradation profiles are, therefore, required to address all the above-mentioned challenges [15].

Among the known biodegradable metals, magnesium (Mg) and iron (Fe) have been studied the most [16,17]. The well-known challenge in developing Mg-based biomaterials concerns their excessively high biodegradation rates [17,18]. Hydrogen released during the biodegradation of Mg alloys is another concern [19]. Fe-based biomaterials, on the other hand, degrade too slowly [20], meaning that the implant stays in the human body longer than necessary and may hinder the process of full tissue regeneration. Moreover, according to the *in vivo* tests of pure Fe stents, voluminous biodegradation products are formed and remain in the human body for long periods after implantation [21,22]. Although developing new alloys and functional coatings could improve the performance of biodegradable Mg and Fe [23,24], an alternative and potentially more rewarding approach would be to develop biomaterials based on the other types of biodegradable metals. Zinc (Zn) and its alloys are considered highly promising candidates for this purpose, as they are capable of tackling some of the fundamental engineering challenges associated with the use of biodegradable Mg and Fe [25]. Zn offers multiple advantages as compared to Mg- and Fe-based biomaterials. First, Zn is one of the most abundant essential trace elements in the human body, confined primarily to skeletal muscles and bones (86%) [26]. Furthermore, over 600 enzymes rely on Zn for proper orientation and function [27]. Moreover, Zn plays catalytic, structural, and regulatory roles in the functions of human cells [28,29]. From this perspective, Zn ions released from the implant could participate in the metabolic activity of the host cells instead of causing systemic toxic side effects [30]. Secondly, the biodegradation process of Zn does not generate hydrogen gas. Thirdly, being similar to Mg but opposed to Fe, the biodegradation products of Zn are biocompatible [31]. Finally, as the chemical potential of Zn falls between the chemical potential values of Mg and Fe, it should exhibit a more suitable biodegradation rate, as compared to fast degrading Mg or slowly degrading Fe [32,33]. Ideally, the biodegradation rate of implants should match the bone regeneration rate, during which the implants provide enduring mechanical support for 3–6 months and fully degrade in 1–2 years [25]. Rapid degradation may compromise the mechanical integrity during the healing process [34], while slow degradation causes long-term implant retention and in turn metabolic complications [21].

However, unlike AM bio-inert titanium or cobalt-chromium, AM biodegradable metals pose many processing challenges, such as severe evaporation and high chemical activity, especially for Mg and Zn [35]. Under any inappropriate processing conditions, defects including voids, lack of fusion, rough surface, severe residual stresses and distortions have been observed. Even for Fe, evaporation was found to play an important role in densification during laser melting [36]. Precise process control is therefore needed in order to obtain eligible samples from AM for further investigation. Up to date, only a few studies on powder bed fusion AM porous biodegradable Mg, Fe, and Zn have appeared in the literature [37–42]. AM

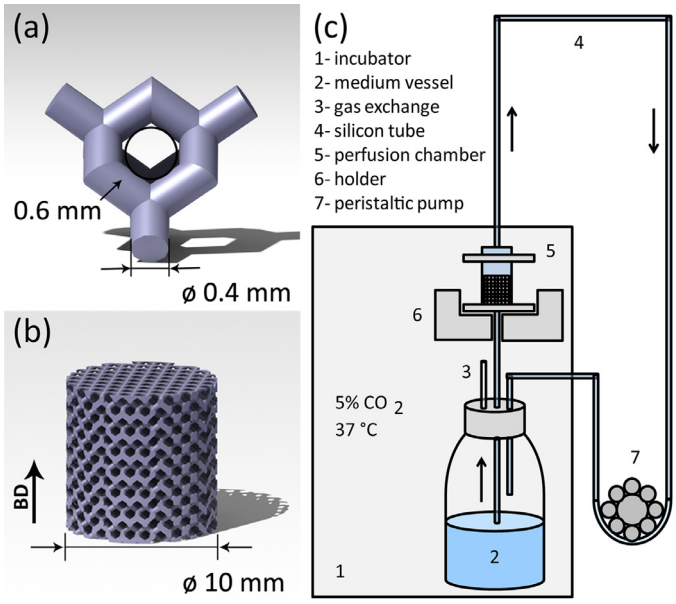

Fig. 1. Topological design of AM porous Zn specimens: (a) diamond unit cell, (b) Zn scaffold, and (c) dynamic degradation setup. BD: building direction.

porous Mg and Fe have both demonstrated unique biodegradation behaviors, as compared to their bulk counterparts [37,38]. However, as AM porous Zn has just been realized [39,43,44], no information regarding its biodegradation, biocompatibility, and mechanical property changes along with its *in vitro* biodegradation is available in the literature. Here, for the first time, we present an integrative study on the static and dynamic biodegradation behavior in a revised simulated body fluid, evolution of mechanical properties with increasing immersion time, electrochemical performance, and biocompatibility of the AM porous Zn.

2. Material and methods

2.1. Scaffold manufacturing

Cylindrical scaffolds (with dimensions of 10 mm in height and 11.2 mm in diameter, Fig. 1a) based on a diamond unit cell (unit cell size: 1.4 mm, strut thickness: 0.4 mm) were designed (Fig. 1b). Specimens were produced by laser powder bed fusion AM (ProX DMP 320 machine, 3D Systems, Belgium). The machine had a maximum laser power of 500 W and could reach oxygen levels below 50 ppm in the build chamber. A nitrogen-atomized Zn powder was used in this study with the following properties: particle sizes: D_{10}: 26 µm, D_{50}: 39 µm, and D_{90}: 60 µm; O content: 2551±81 ppm, N content: 17±2 ppm, and H content: 7.6 ± 0.8 ppm. The morphology of powder particles was analyzed before [45]. The powder layer thickness was 60 µm and the energy density 39.0 J/mm^3. The specimens were removed from the steel baseplate by wire electrical discharge machining (WEDM). 96% ethanol was used to ultrasonically remove powder particles entrapped in the pores of the specimens for 20 min. Subsequently, the specimens were cleaned by using a solution composed of 5% (by volume) hydrochloric acid, 5% nitric acid, and 90% ethanol for 2 min to further remove loose powder particles, after which 96% ethanol was used again to wash away residual hydrochloric acid.

2.2. Morphological characterization

Micro-computed tomography (µCT) was used to scan the Zn scaffolds (Phoenix Nanotom, GE SensingInspection Technologies

GmbH, Germany) with the following parameters: 220 µA tube current, 130 kV tube voltage, 500 ms exposure time,12 μm^3 resolution, and1440 projections. Phoenix Datos|x 2.0 (GE Sensing & Inspection Technologies GmbH, Germany) was used to reconstruct and transform the acquired data into 2D images (*i.e.*, DICOM image stacks). To extract quantifiable data from these images, the following steps were taken. First, the images were locally thresholded (FIJI, NIH, Bethesda, MD, USA) over a range of 107 to 255 for the Zn material. Then, circular regions of interest (ROIs) (diameter: 10 mm) were outlined to include all the structures. BoneJ (a plugin of FIJI) was used to calculate the porosity, pore size, and average strut thickness of the AM porous Zn. Furthermore, the weighing method was applied to determine the porosity: $Porosity = 1\text{-}(W_{Zn}/V_{bulk})/\rho_{Zn}$, where W_{Zn} and V_{bulk} are the weight and apparent volume of the specimen, respectively, and ρ_{Zn} is the theoretical density of pure Zn. The porosity within the struts was determined by using a method based on Archimedes' principle [11].

After the biodegradation tests, two different ranges, *i.e.*, 45–107 and 107–255, were applied to segment the biodegradation products and porous Zn structure, respectively. After segmentation in FIJI, the volume of Zn and that of the biodegradation products were calculated with BoneJ (a plugin of FIJI). The images were then exported for 3D reconstruction (AVIZO Fire, VSG, France).

2.3. Microstructural characterization

Electron back-scattered diffraction (EBSD) was conducted with an HKL Nordlys II detector, attached to a field emission gun scanning electron microscope (FEGSEM) (JEOL JSM-6500 F, Japan), at 200 nm step size. TSL OIM® Analysis (EDAX Inc.,USA) was used to reconstruct inverse pole figure (IPF) maps. The average grain width was calculated by using the line intercept method, according to ASTM E112-12. Pole figures (PF) with (0001) and (1010) reflections were measured. EBSD specimens were ground, mechanically polished up to 1 µm with lubricant, followed by further mechanical polishing with 0.04 µm silica.

2.4. Static and dynamic immersion tests

Static *in vitro* immersion tests were performed inside an incubator (5% CO_2, 20% O_2, 37 °C) using 300 ml revised simulated body fluid [46] (r-SBF), *i.e.*, a r-SBF volume to sample surface (25 cm^2) ratio of 12, for up to 28 days. In addition, dynamic *in vitro* immersion tests were performed in r-SBF up to 28 days using a self-designed bioreactor (5% CO_2, 20% O_2, 37 °C) (Fig. 1c) at a unidirectional flow rate of 0.3 ml/min [47–49]. Medium pH values were registered (InLab Expert Pro-ISM, METTLER TOLEDO, Switzerland) at 1, 2, 7, 14, and 28 days of static and dynamic biodegradation. An inductively coupled plasma optical emission spectroscope (ICP-OES, iCAP 6500 Duo, Thermo Scientific, USA) was used to determine the concentrations of Zn, Ca, and P ions in the medium. All the tests were performed in triplicate.

2.5. Characterization of the biodegradation products

The morphologies and compositions of the biodegradation products were analyzed using a scanning electron microscope equipped with an energy-dispersive X-ray spectroscope (EDS) (SEM, JSM-IT100, JEOL, Japan). To observe the biodegradation layer of the specimens, a dualfocused ion beam(FIB) available as part of a scanning electron microscope setup (FIB-SEM) (Helios G4CX, FEI, The Netherlands) was used for cross-section milling and EDS mapping. The cross-section milling was performed at a tilting angle of 52° with a Ga ion beam operated at 30 kV over a current range of 0.5 to 20 nA.

For the analysis of the biodegraded specimens, Fourier-transform infrared spectroscopy (FTIR) spectra were collected at 4 cm^{-1} resolution over 128 scans for each spectrum, using a Thermo-Nicolet Nexus FTIR (USA) apparatus. Prior to the analysis of the biodegradation products, a background spectrum was collected from a sample before biodegradation. The final spectra were subtracted from this background. Moreover, an X-ray diffractometer (XRD, Bruker D8 Advance diffractometer in Bragg-Brentano geometry, Germany) was used for the identification of the phases in the biodegradation products. The diffractometer was operated at 45 kV and 40 mA (power: 1.8 kW) using Cu Ka radiation with 0.035° step size and 10 s dwell time per step. In addition, X-ray photoelectron spectroscopy (XPS, Thermo Fisher Scientific, K Alpha model, USA) was used to characterize the surface chemical states of the specimens following the biodegradation tests. The XPS measurements were performed under normal emission at 250 µm spot size and at 10^{-8} mbar base pressure using a monochromated Al Kα X-ray source.Thermo Avantage v5.903 software (Thermo Fisher Scientific, USA) was used to process and analyze the spectra.

2.6. Electrochemical tests

AM porous Zn specimens were mounted in an epoxy resin and ground using 2000 grit SiC sandpapers for electrochemical tests. Surface area (*i.e.*, 0.28 cm^2) of the specimen exposed to the electrolyte was measured by using ImageJ (NIH, Bethesda, MD, USA). Specimens were made conductive by placing copper screws inside the resin. Electrochemical tests were performed in r-SBF at 37 °C with a Bio-Logic SP-200 potentiostat (Bio-LogicScience Instruments, Claix,France). A three-electrode electrochemical cell was set up with Zn specimen as the working electrode, graphite as the counter electrode, and a saturated calomel electrode as the reference electrode. Potentiodynamic polarization (PDP) measurement was performed after the open circuit potential (OCP) was reached and stabilized for 2 h. Afterwards, the specimen was polarized from −0.2 V to +0.5 V potential *versus* OCP at 0.5 mV/s scan rate. For electrochemical impedance spectroscopy (EIS), the tests were repeated at 1, 2, 7, 14, 21 and 28 days with 10 mV amplitude within a 100 kHz to 10 mHz frequency range. The impedance data were analyzed with the EC-Lab software (Bio-LogicScience Instruments, Claix,France) and fitted to the equivalent electrical circuits, where R_s represented the solution resistance; R_f and constant phase element CPE_f were applied to describe the resistance and non-ideal capacitance properties of the biodegradation film, respectively; the charge transfer resistance R_{ct} and the constant phase element representing the non-ideal double layer capacitance CPE_{dl} in parallel were used to describe the electrochemical interface of the electrolyte solution and the Zn substrate. The linear polarization resistance (LPR) of the samples was also measured consecutively at different immersion time points at ± 15 mV *versus* OCP at 0.167 mV s^{-1} potential sweep rate. The tests were performed in triplicate.

2.7. Mechanical characterization

Compression tests were carried out at 2 mm/min (10 kN, Instron,Germany). The specimens had a height of 10 mm and a diameter of 11.2 mm. The yield strengths and quasi-elastic gradients (elastic modulus) of the AM porous Zn specimens before and after the immersion tests were determined according to ISO 13,314:2011 [38]. The tests were performed in triplicate.

Hardness was measured by using a microhardness tester (DuraScan, G5, Austria) at 1 N indentation load. Three tests were carried out on the cross section of the AM Zn substrate and another three indentations on the biodegradation products.

Table 1
Topological characteristics of AM Zn scaffolds.

AM Zn scaffold	Strut size (μm)	Pore size (μm)	Porosity
Design	400	600	67%
Micro CT	441±1	550±38	62±2%
Weighing method	–	–	60±1%

2.8. Cytocompatibility

Human osteoblast-like cells (MG-63, ATCC, CRL-1427) were cultured in 10% fetal calf serum (PAN Biotech) containing Dulbecco's modified eagle medium with low glucose 100 mg/L (DMEM LG) (Sigma) under physiological conditions (5% CO_2, 20% O_2, and 95% humidity) at 37 °C. The biocompatibility of AM porous Zn specimens were evaluated through direct cell seeding and indirect extract-based cytotoxicity tests. Cleaned specimens were sterilized in 100% isopropanol (Merck; Darmstadt, Germany) for 30 min.

Extracts were prepared at 0.2 g/ml concentration by incubating the specimens in the DMEM LG medium with serum for 72 h under physiological conditions, as recommended in EN ISO standards 10,993:5 and 10,993:12. Prepared 1x extract was diluted to 10x using the same medium. A 1x extract from AM Ti-6Al-4 V porous scaffolds of the same dimensions served as control. All the extracts were sterile filtered (0.2 μm). 20% Dimethyl sulfoxide (DMSO) was used as the positive control. The methodology followed for the preparation of the extracts and MTS assay was the same as that previously reported by us [38]. After MG-63 cells reached optimal adherence, the serum-containing DMEM LG medium was replaced with 10x extracts and cells were further incubated for 0, 24, 48 and 72 h under physiological conditions. Relative cellular activity was tested using CellTiter 96® AQueous One Solution Cell Proliferation Assay (G3580, Promega,USA) [37].

Previously cleaned and sterilized specimens were seeded with 3×10^6 MG-63 cells and incubated for 24 h in the serum-containing DMEM LG medium under physiological conditions. Cell-seeded specimens were cut longitudinally (Figure S1a) and stained using Live and Dead Dye from Live and Dead Cell Assay kit (ab115347, Abcam, UK). A 5x concentration of the dye was added to the specimens with cells and then incubated at room temperature for 10 min. The cells were analyzed by fluorescent optical imaging first and the same specimens after rinsing in 1X phosphate buffered saline were fixed and used for SEM analysis (ESEM XL 30 FEG, FEI, Eindhoven, The Netherlands) [37].

2.9. Statistical analysis

A two-way ANOVA test ($\alpha = 0.05$) and a post-hoc test (*i.e.*, Tukey's multiple comparison test, $\alpha = 0.05$) were run to analyze the relative cytotoxicity ($p < 0.0001$, ****; $p < 0.001$, ***; $p < 0.01$, **; $p < 0.05$, *; *n.s.* = not significant).

3. Results

3.1. Macrostructure and microstructure of the specimens

The average strut size and pore size of the as-built scaffolds were 441 ± 1 μm (design value = 400 μm) and 550 ± 38 μm (design value = 600 μm), respectively (Table 1). The porosity of the specimens was calculated to be 62 ± 2% (μCT) or 60 ± 1% (dry weighing) (Table 1). The relative density of the struts was measured to be 93.6 ± 0.7%. Columnar grains along the building direction were observable from the IPF mapping on the longitudinal section of the struts (Fig. 2a). The average width of the elongated grain was about 16.0 ± 1.6 μm. On the cross section of the AM porous Zn specimens, no extraordinary grain growth morphology could be recognized (Fig. 2c). On both the longitudinal and cross sections, the (0001) PF and $(10\bar{1}0)$ PF did not show obvious preferred grain growth in the building direction (Fig. 2b and d).

3.2. In vitro biodegradation behavior of the specimens

During both dynamic and static immersion tests, white biodegradation products were gradually generated on the surface of the struts, as immersion time increased (Fig. 3a). However, the dynamic biodegradation tests appeared to produce more biodegradation products than the static ones. Interestingly, the biodegradation products mainly formed at the bottom of the specimens (attached to the beaker) under the static condition, but on the top of the specimens (the outlet side of the medium flow) under the dynamic condition (Fig. 3a).

The pH value remained stable around 7.5 and 7.6 during both static and dynamic biodegradation tests up to 14 days, and increased during the dynamic tests to 7.7 at day 28 (Fig. 3b). Under the static condition, the concentration of Zn ion slightly increased from 0.11 to 0.25 mg/L after 28 days. In contrast, the specimens tested under the dynamic condition exhibited higher Zn ion concentrations (as compared to those tested statically) at day 2, which further increased to 4.9 mg/L at day 28 (Fig. 3c). Over this period, the concentrations of P and Ca ions decreased under both conditions (Fig. 3d and e). The P and Ca ion concentrations were always lower under the dynamic test condition as compared to the static test condition (Fig. 3d, e).

3.3. Characteristics of the biodegradation products on the scaffolds

White particles gradually formed on the surfaces of the biodegraded specimens (Fig. 4a–c) along with increasing immersion time. After 1 day, small-size, white biodegradation products appeared on the surface of the specimens (Fig. 4d), which contained Zn, C, O, P, and Ca (Fig. 4d, inlay) according to EDS. At day 14, the white biodegradation products with a spherical morphology had grown in size, while the P and Ca contents in these products were increasing (Fig. 4e, inlay). At day 28, the biodegradation layer became increasingly compact, while the O, P, and Ca contents increased further (Fig. 4f, inlay). EDS mapping on the FIBed section allowed for the analysis of elemental distribution across the biodegradation layer (Fig. 4g), revealing that O had formed earlier (adjacent to the Zn substrate), followed by P and Ca. C was mainly present at the top of the biodegradation layer (Fig. 4g). XRD analysis showed the presence of ZnO, $Zn_5(CO_3)_2(OH)_6$, $Ca_3(PO_4)_2$, and $Zn_5(OH)_6Cl_6{\cdot}H_2O$ at day 1, with increased intensities of these biodegradation products at day 28 (Fig. 4h). The FTIR spectrum with peaks at 1040 and 1650 cm^{-1} revealed the presence of PO_4^{3-} and HPO_4^{2-} (Fig. 4i), respectively [50], while the broad band from 1400 to 1550 cm^{-1} likely resulted from CO_3^{2-} [51]. HPO_4^{2-} absorption peaks emerged from day 7 and increased onwards, together with the increases of CO_3^{2-} and PO_4^{3-} peaks.

The total spectrum of XPS revealed that the biodegradation products were composed of Zn, O, C, P, Ca, Na, Mg, S, N, and Cl (Fig. 5a). Although there were no differences in the types of the elements between the different immersion time points, with increasing immersion time, the percentages of Ca, O, and P increased, while the percentage of Zn decreased. In addition, high-resolution XPS spectra of Zn2p3/2, C1s, and P2p were collected from the surfaces of the specimens and fitted. The peaks located at 1022 and 1024 eV might be attributed to ZnO and $Zn(OH)_2$, respectively (Fig. 5c,d) [52]. The atomic percentage of ZnO increased from 0.28 at day 1 (Fig. 5c) to 0.50 at day 28 (Fig. 5d). As for C1s, the peaks were well fitted with three signals at 284, 286, and 288 eV (Fig. 5d, e). The 284 eV signal was assigned to C–C bonds, while the 286 and 288 eV signals were attributed to C–O and $C=O$, respectively

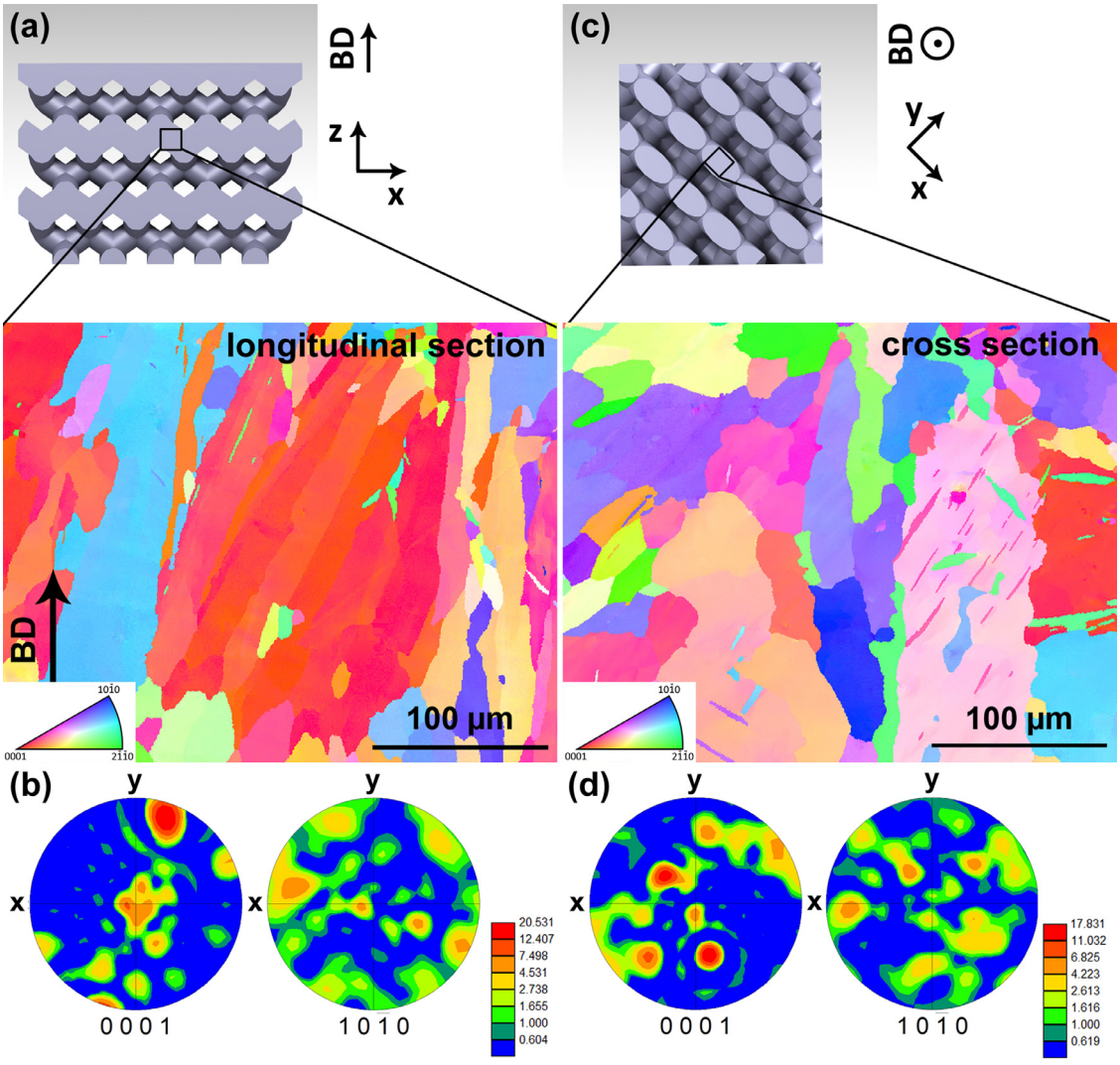

Fig. 2. EBSD characterization of the struts of AM Zn specimens: (a) IPF map and (b) PF on the longitudinal section, (c) IPF map and (d) PF on the cross section. BD: building direction.

[53,54]. The atomic percentage of $C=O$ also increased from 0.10 at day 1 to 0.14 at day 28. Finally, the P2p peaks observed at about 133 and 134 eV (Fig. 5f) could be characterized to be PO_4^{3-} and HPO_4^{2-}[55].

In addition to mostly homogeneous biodegradation profiles, we found several localized biodegradation spots within the AM porous Zn specimens (Fig. 6). A crystal-like morphology was observed at these spots and EDS analysis revealed a high percentage of Cl in these areas (Fig. 6a, b). EDS mapping (Fig. 6d) also showed the accumulation of Cl at the localized biodegradation sites on the cross-section of the biodegradation layers (Fig. 6c).

3.4. Electrochemical responses

According to the PDP results (Fig. S2), the corrosion current density of the AM porous Zn was 45 ± 2 μA/cm^2. The biodegradation rate was calculated to be 0.67 ± 0.04 mm/year based on ASTM G59. According to the Nyquist plots (Fig. 7a), the diameter of the capacitive loop increased after 7 days of immersion, and then decreased from day 14 to day 21, followed by further growth afterwards. The Bode plots (Fig. 7b, c) showed similar trends of impedance modulus at the 0.01 Hz (low) and 10 Hz (medium) frequencies. According to the data resulting from the fitted equivalent circuit for the AM porous Zn specimens (Fig. 7a, Table 2), R_f and R_{ct} gradually increased until day 14, decreased after day 14, and increased again after day 21. The LPR value showed a trend similar to the values of R_f and R_{ct} (Fig. 7d).

3.5. Mechanical properties

Under compression, the AM porous Zn showed smooth stress-strain curves (Fig. 8a) with no abrupt drop even after biodegradation for 4 weeks. Following a similar trend, the curves all began with a steep slope in the elastic region. Afterwards, the stress decreased substantially and then a plateau stage appeared with almost no fluctuations (Fig. 8a). Interestingly, after 28 days of dynamic biodegradation, the yield strength of the AM porous Zn gradually increased from 11.8 to 13.9 MPa (Fig. 8b). While the yield strengths of the specimens undergoing static biodegradation were lower than those exposed to dynamic biodegradation, they were higher than the yield strength of the as-built specimens (10.8 MPa), even after 28 days (12.0 MPa). The elastic modulus of the AM porous Zn increased at day 1, but decreased afterwards (Fig. 8c). Similarly, the elastic modulus of AM porous Zn after 28 days of dynamic biodegradation (879.3 MPa) was higher than that of the as-built specimens (785.7 MPa).

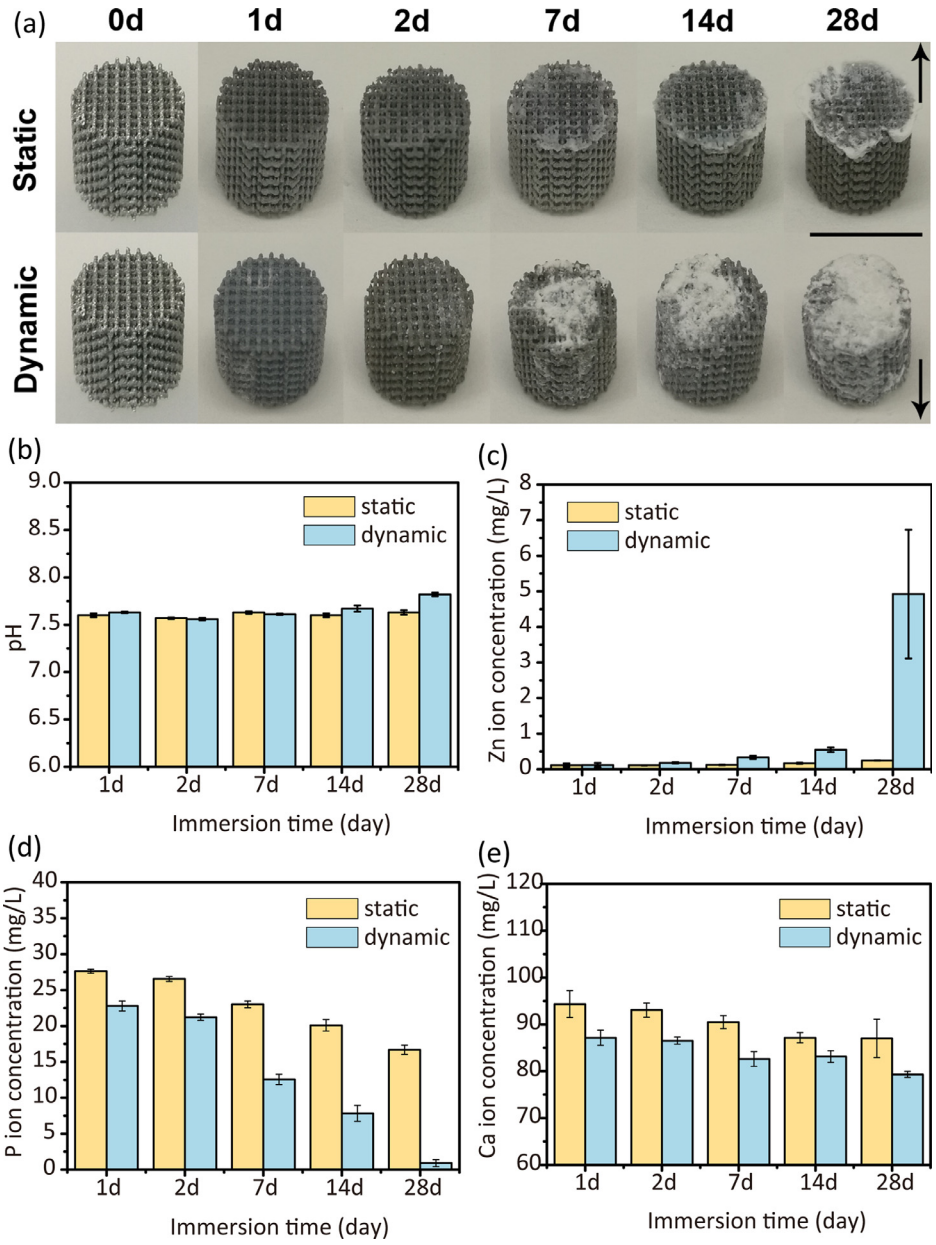

Fig. 3. Biodegradation behavior of AM porous Zn: (a) visual inspection of the as-degraded scaffolds, (b) pH variation with immersion time, (c) Zn ion concentration variation with immersion time, (d) P ion concentration variation with immersion time, and (e) Ca ion concentration variation with immersion time. Arrow in (a) points to the bottom side of the scaffolds during degradation. Building direction is opposite to the arrow. Scale bar in (a): 1 cm.

Table 2
EIS fitting parameters of AM Zn after immersion tests at different time points.

Immersion time	R_s Ω•cm^2	CPE_f 10^{-6}• Ω^{-1}•cm^{-2}•s^{n1}	n_1	R_f Ω•cm^2	CPE_{dl} 10^{-4}• Ω^{-1}•cm^{-2}•s^{n2}	n_2	R_{ct} Ω•cm^2	Chi-square 10^{-3}
1d	6.0 ± 0.1	10.1 ± 0.2	0.88	669±17	8.2 ± 3.6	0.60	99±16	1.1
2d	6.5 ± 0.1	8.3 ± 0.2	0.85	642±6	3.4 ± 0.4	0.82	154±6	0.9
7d	4.9 ± 0.2	3.4 ± 0.1	0.83	1389±10	5.1 ± 0.3	0.65	616±16	0.9
14d	5.3 ± 0.2	4.2 ± 0.1	0.81	1303±15	4.4 ± 0.5	0.61	504±17	1.3
21d	7.9 ± 0.1	5.6 ± 0.1	0.83	902±5	9.0 ± 0.1	0.85	110±6	1.0
28d	8.3 ± 0.1	9.9 ± 0.1	0.79	1137±6	13.0 ± 0.2	0.90	129±8	0.7

The average hardness value of the degradation products was 197 ± 4 HV, while the value of the AM Zn was 41 ± 3 HV.

3.6. Surface morphology of specimens after biodegradation

When the as-built specimens were segmented using a threshold range of 107 to 255, the total volume of the scaffolds was 345.2 ± 0.5 mm^3. After 28 days of biodegradation, this value decreased to, respectively, 332.1 ± 2.3 mm^3 and 319.0 ± 3.4 mm^3 (*i.e.*, 3.6% and 7.8% of weight reduction or 0.07 and 0.13 mm/year) under the static and dynamic conditions. The AM Zn scaffolds appeared to have experienced a higher degree of localized biodegradation under the static condition (Fig. 9, square), while the dynamic flow resulted in more homogeneous biodegradation. Quantification of

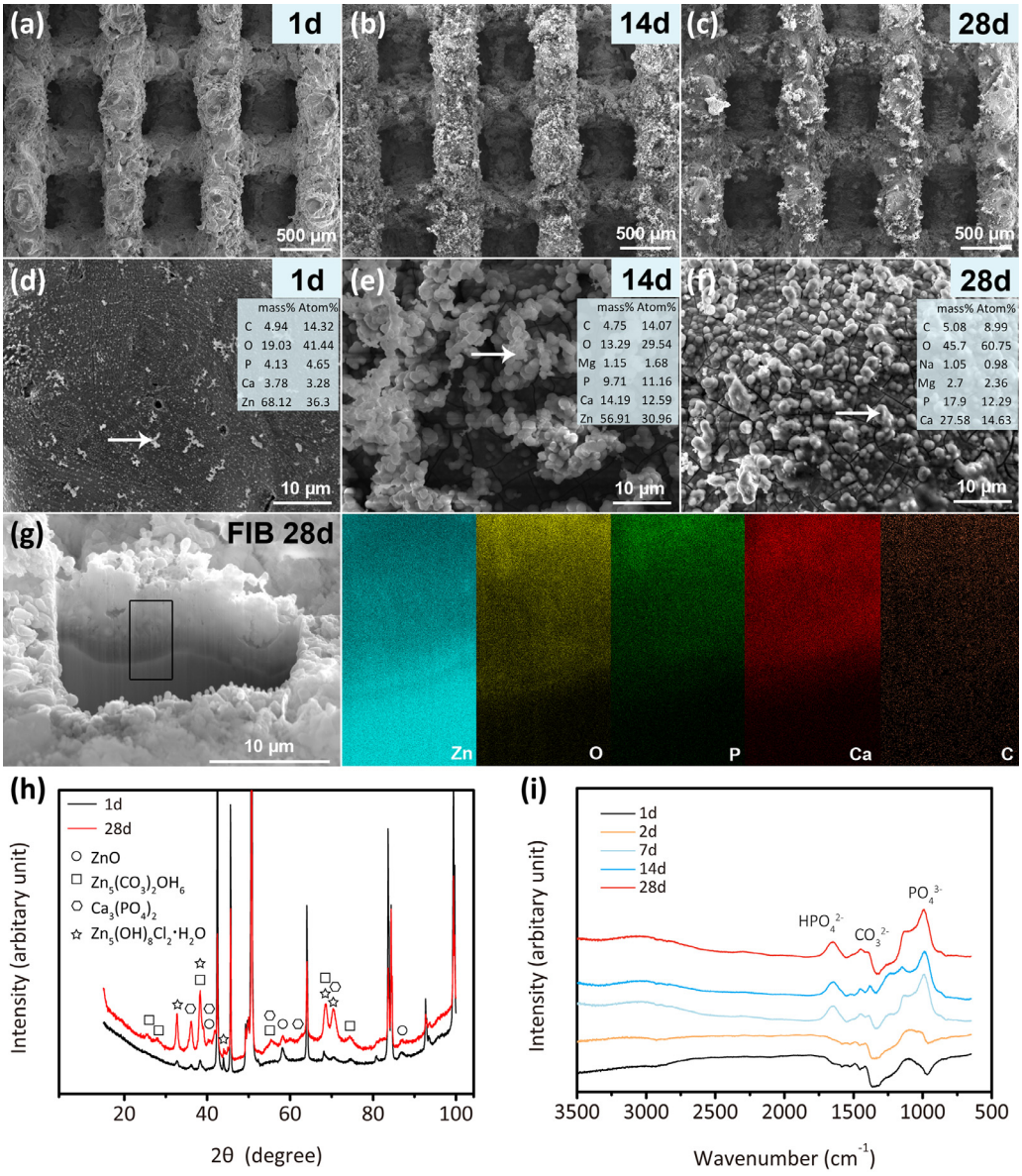

Fig. 4. Biodegradation product analyses of AM porous Zn: (a), (b) and (c) SEM images of degradation products at day 1 (a), day 14 (b), and day 28 (c), (d), (e) and (f) higher magnification SEM images and EDS analyses at day 1 (d), day 14 (e), and day 28 (f), (g) FIB and EDS mapping of the degradation layer at day 28, (h) XRD analysis, and (i) FTIR analysis of degradation products. Arrow: EDS point analysis. Square: EDS mapping area.

the biodegradation products using a threshold range that separated Zn and the biodegradation products from each other showed that the dynamic condition resulted in a larger volume of biodegradation products ($104 \pm 9\,mm^3$), as compared to that for the static condition ($59 \pm 8\,mm^3$) (Fig. 9). Furthermore, the biodegradation products appeared to have mostly formed on a specific side of the specimens, which depended on the test condition, as well as in the center (Fig. 9). Under the static test condition, the biodegradation products mainly formed on the bottom side of the specimens, which was in contact with the beaker (Fig. 9, arrow). Under the dynamic test condition, however, the biodegradation products were found more on the top side of the specimens, which was the outlet side of the r-SBF flow (Fig. 9).

3.7. In vitro *cytotoxicity*

The metabolic activity of MG-63 cells cultured with the extracts from the AM porous Zn specimens was assayed and compared to that of the extracts from AM Ti-6Al-4 V specimens (positive controls). Both extracts, from Zn and Ti-6Al-4 V, resulted in around 95% cellular activity after 24 and 48 h, thus exhibiting level 0 cytotoxicity (*i.e.*, < 25%),according to ISO 10,993. Even after 72 h of incubation, a large fraction of MG-63 cells cultured in the Zn extracts were viable (*i.e.*, 85%), conforming to a high level of cytocompatibility (*i.e.*, level 0 cytotoxicity). In contrast, cellular activity in the negative DMSO controls dropped quickly to ≈ 55% after 24 h and to ≈15% after 72 h (Fig. 10a).

3.8. *Biocompatibility* in vitro

Live-dead staining of MG63 cells showed that most of cells were viable (fluorescing green) even after 24 h of direct contact with the AM porous Zn specimens (Fig. 10b). The number of cells with compromised cell membrane integrity (yellow-red) was similar to the gold standard biomaterial (*i.e.*, Ti-6Al-4 V).

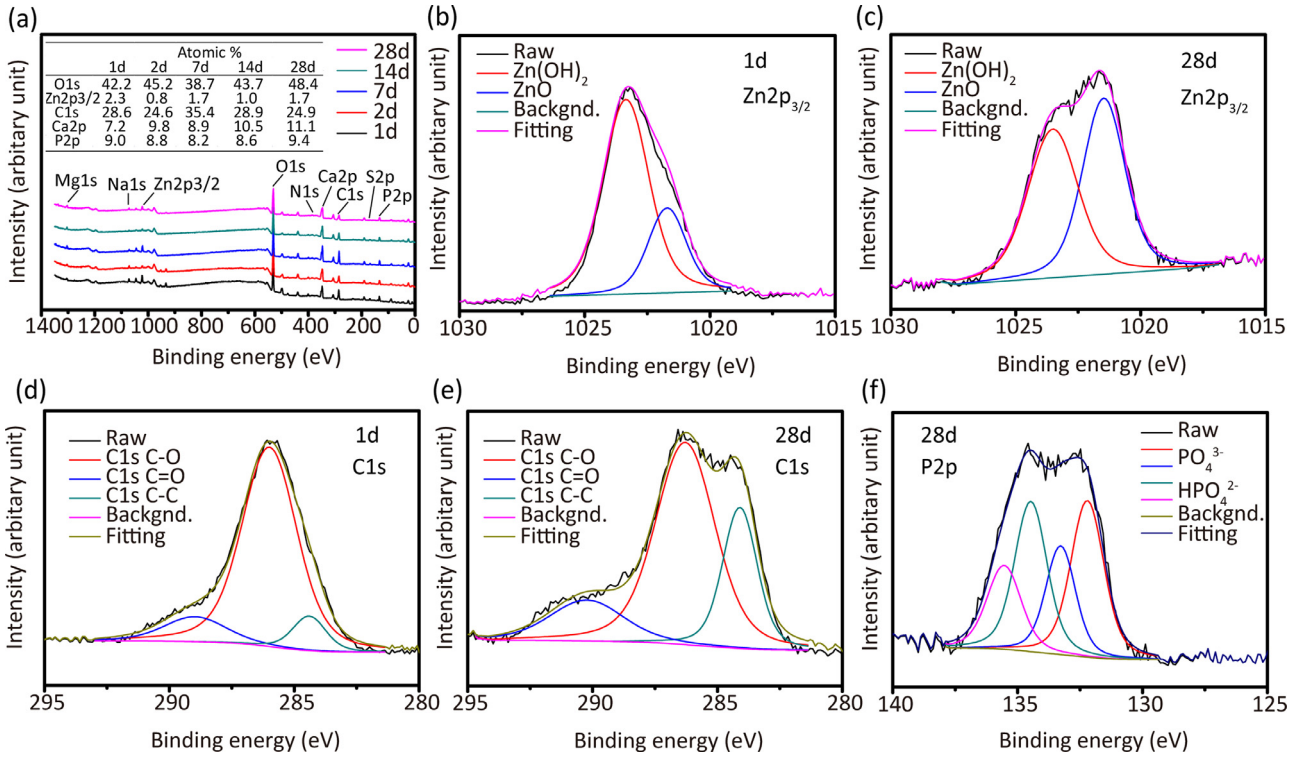

Fig. 5. XPS spectra of AM porous Zn after degradation: (a) total spectrum, (b) and (c) $Zn2p_{3/2}$ peaks at day 1 (b) and day 28 (c), (d) (e) C1s peaks at day 1 (d) and day 28 (e), (f) P2p peaks at day 28.

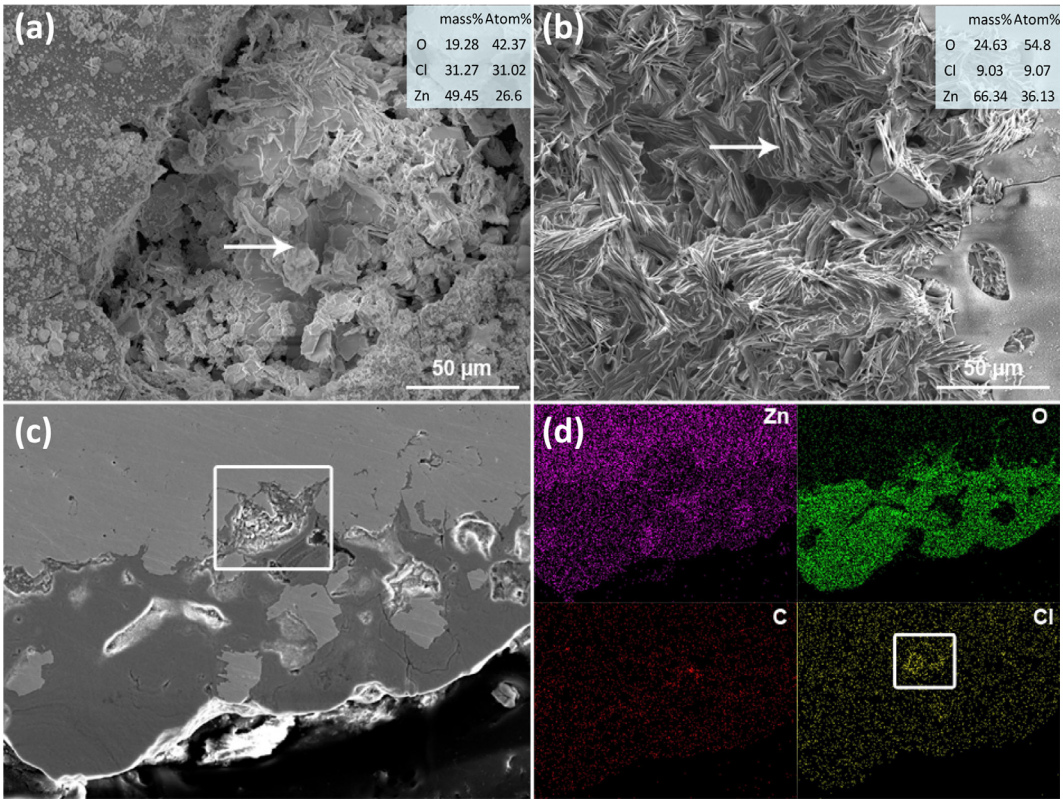

Fig. 6. Localized degradation of AM porous Zn after degradation at day 28: (a) (b) morphology of localized degradation and EDS point analysis, (c) cross section of localized degradation, and (d) EDS mapping. Arrow: EDS point analysis. Square: localized degradation.

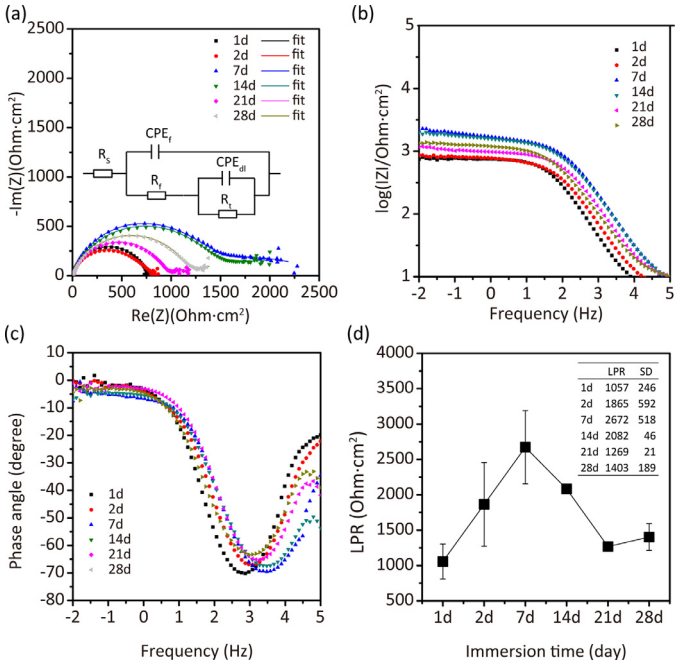

Fig. 7. Electrochemical characterization of AM porous Zn after immersion tests at different time points: (a) Nyquist plots and equivalent circuits, (b) Bode plots of impedance modulus |Z| *vs.* frequency, (c) Bode plots of phase angle *vs.* frequency, and (d) LPR variation with immersion time.

MG-63 cells had intimate contact with the struts of the AM porous Zn with far-stretching filopodia-like protrusions (Fig. 10c), similar to their phenotype on Ti-6Al-4 V. Cells not only were distributed around the periphery of the scaffolds but also colonized the inner core, as evident from the cross-sectional images (Fig. S1b).

4. Discussion

The AM porous Zn showed great potential to meet the three basic requirements of bone scaffolds: (i) the Zn scaffolds had sufficiently high mechanical properties, particularly elastic moduli during the 28-day biodegradation ($E = 700–1000$ MPa), to provide mechanical support, as these values are comparable with those reported for cancellous bone ($E = 10–2000$ MPa [56]). Surprisingly, the mechanical properties of the AM porous Zn even increased after four weeks of *in vitro* immersion; (ii) the Zn scaffolds had high porosity, totally interconnected pores and high-precision unit cell geometry; (iii) the AM porous Zn specimens showed a very promising biodegradation rate (≈7.8% volume loss after 4 weeks), which is an intermediate value between fast degrading Mg-based alloys and slowly degrading Fe-based alloys. This intermediate rate of biodegradation is deemed appropriate for most skeletal applications where wound healing is expected to complete within six months to one year. From a biological viewpoint, AM porous Zn showed good cytocompatibility, based on a high degree of cell viability and the intimate contact between MG-63 cells and the specimen surface.

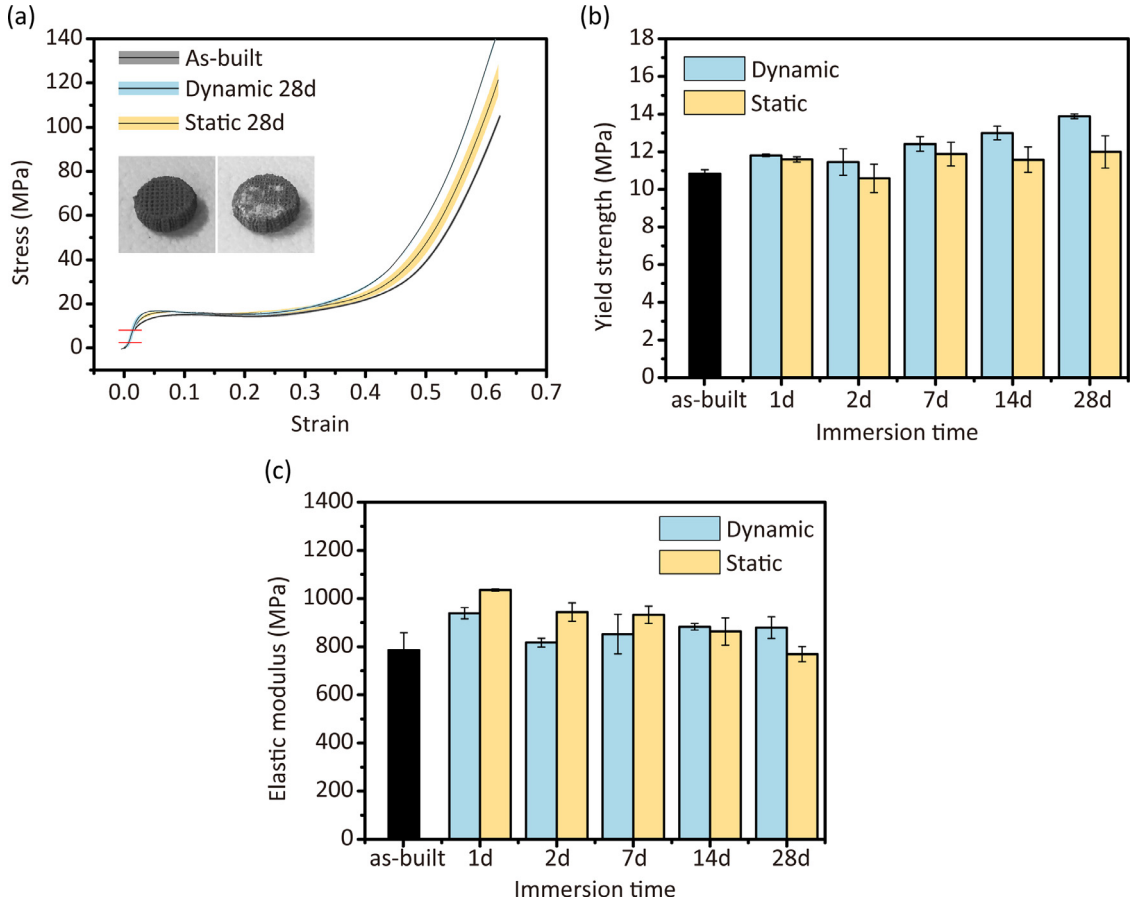

Fig. 8. Mechanical behavior of AM porous Zn: (a) compressive stress-strain curves of Zn scaffolds before and after 28 days of degradation, (b) yield strength change with immersion time, and (c) elastic modulus change with immersion time. Red line in (a) indicated the elastic region (For interpretation of the references to colour in this figure legend, the reader is referred to the web version of this article.).

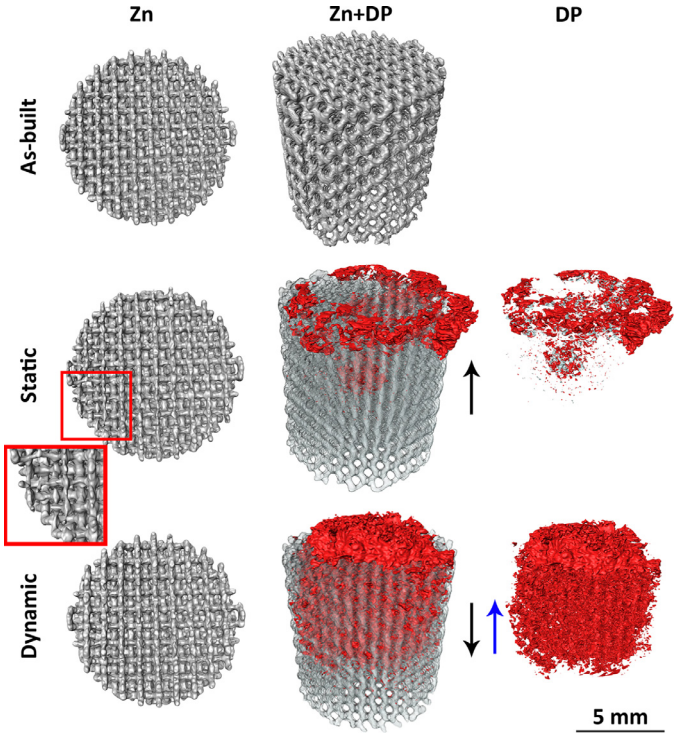

Fig. 9. Micro-CT analysis of AM porous Zn after 28 days immersion. DP: degradation products. Square: localized degradation. Grey: Zn. Red: biodegradation products. Black arrow points to the bottom side of the scaffolds during degradation. Blue arrow indicates the flow direction for dynamic tests. Scale bar: 5 mm (For interpretation of the references to colour in this figure legend, the reader is referred to the web version of this article.).

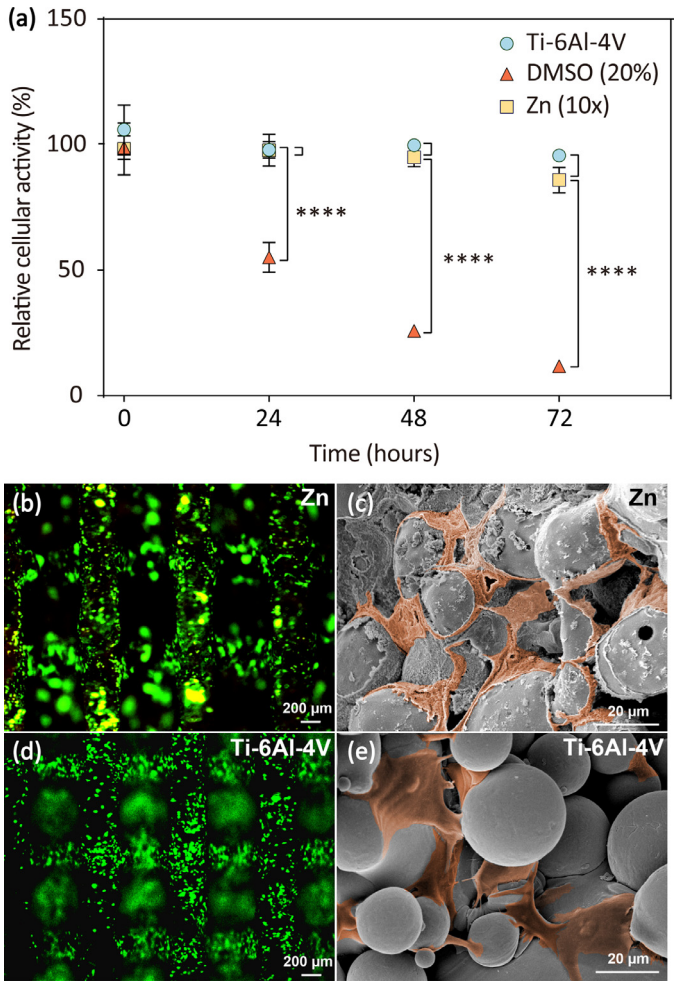

Fig. 10. Biocompatibility and cytotoxicity of AM porous Zn *in vitro*: Remaining cellular activity of MG63 cells upon exposure to Zn scaffolds (a), as measured by MTS assay. Experiments were performed with extracts of randomly chosen replicate scaffolds ($n=5$) and analyzed in at least technical triplicates (Zn, $n=5$; Ti-6Al-4 V, $n=3$). Fluorescent optical images (FOI) of cells attached to AM Zn scaffolds after 24 h (b) and AM Ti-6Al-4 V scaffolds (d). SEM images of cells attached to AM Zn scaffolds after 24 h (c) and AM Ti-6Al-4 V scaffolds (e). Brown masks indicate individual cells. (For interpretation of the references to colour in this figure, the reader is referred to the web version of this article.)

4.1. Microstructural features

Refined grains (Fig. 2) in the as-built Zn can be attributed to the high cooling rates (10^3–10^8 K/s) during laser powder bed fusion [57], which is similar to the observation of AM Zn reported by other researchers [39]. Fine grains can improve the mechanical performance of AM porous Zn. The elongation of the grains along the building direction was caused by the thermal gradients experienced during the process of layer-by-layer laser melting [58]. During the laser powder bed fusion process, the melting layer and the previous layer has the same chemical composition. New phase nucleation is not required for grains to grow epitaxially further from the substrate layer [59]. The direction of grain growth depends on the maximum heat transfer direction during solidification, which is perpendicular to the melt pool boundary. Thus, elongated grains along the building direction were observed in the AM porous Zn. Considering the relative density of the struts being 93.6 ± 0.7%, further AM process optimization is needed to improve the relative density of the struts. Since the internal pores within the struts can act as the sources of fracture and pitting corrosion, the mechanical properties and biodegradation behavior of AM biodegradable porous Zn can be affected by the sizes, number density and distribution of such pores.

4.2. In vitro *biodegradation characteristics*

In order to better mimic the *in vivo* environment, we developed a dynamic biodegradation set-up (Fig. 1c) and compared the dynamic biodegradation behavior of AM porous Zn with its static degradation behavior. During 28 days of immersion, pH value stayed almost unchanged (around 7.6), meaning that AM Zn degraded slowly and 5% CO_2 worked effectively as a buffer. As the dynamic biodegradation process progressed, the accumulation of OH^- caused a slight increase of the pH value (*i.e.*, to 7.7 at 28 days) (Fig. 3b). According to the ICP results, the dynamic flow of r-SBF increased the biodegradation rate of the AM porous Zn (Fig. 3c). Under the dynamic condition, the surface of the AM porous Zn specimens was constantly washed by the medium. The circulation of the medium over the surface of the specimen inhibited local pH increase, thereby increasing the rate of biodegradation [60]. However, the concentration of Zn ions measured at day 28 (under the dynamic condition) was only 4.9 mg/L (Fig. 3c), which equaled to 1.47 mg of released Zn for 300 mL medium. This value was much lower than the volume reduction (*i.e.*, a volume loss of 7.8%) of 178 mg released Zn (equivalent to 0.13 mm/year) determined using the µCT analysis. The main reason for this difference could be the participation of Zn ions in the formation of the biodegradation products. The white biodegradation products (Fig. 3a) indeed contained Zn, according to the EDS analysis (Fig. 4d-g). XRD also confirmed the presence of Zn oxide on the surface of the AM porous Zn specimens after *in vitro* immersion (Fig. 4h). The biodegradation rate was the highest from the PDP tests, being 0.67 mm/year. Based on this rate, the weight reduction of the AM porous Zn

would be 917 mg (36.7% reduction) after 28 days. As an accelerated test, PDP can only represent a snapshot of biodegradation at the time when it is performed [61,62], *i.e.,* 2 h after immersion in the present case, which means that Zn still had a relatively fresh surface. Moreover, when the PDP tests were performed, the surface of the specimens had experienced a strong polarization effect [63]. Nevertheless, as a straightforward and quantitative technique, PDP can be of help in designing or screening of Zn-based materials before time-consuming immersion tests and *in-vivo* tests [61].

Compared to the results obtained by other researchers using PDP, the AM porous Zn specimens studied here showed a higher rate of biodegradation (*i.e.*, 0.67 mm/year) than the conventionally manufactured ones (*i.e.*, 0.025–0.325 mm/year) [62,64–70]. This might be attributed to the grain refinement and more grain boundaries caused by the laser processing, which could increase the biodegradation rate of pure Zn. However, the effect of grain size on the biodegradation rate of Zn has not yet been studied. It is therefore suggested that further studies are needed to establish a quantitative relationship, particularly given the fact that laser-based AM processes may then be used as a way to tune the biodegradation rate of AM porous Zn. According to the immersion tests, the rate of Zn biodegradation found in this research (0.07 and 0.13 mm/year under static and dynamic condition, respectively) is comparable with the values reported by other researchers in their *in vitro* static immersion tests (*i.e.*, 0.011–0.084 mm/year [62,64,67,70–74]). The static biodegradation rate of the AM porous Zn falls between the values of the AM porous Mg (0.23 mm/year) and Fe scaffolds (0.03 mm/year) [37,38], confirming its moderate degradation profile. Furthermore, it is interesting to note that, for pure Zn, the results of *in vitro* biodegradation tests are consistent with those of *in vivo* tests (0.010–0.065 mm/year) [31,75–80]. It should, however, be noted that in most of the *in vivo* tests the pure Zn wires or stents used for those measurements were implanted in abdominal aorta. Obviously, it is important to find the *in vivo* biodegradation rate of AM porous Zn as a bone implant and its interactions with the surrounding tissues.

4.3. *Static and dynamic* in vitro *biodegradation mechanisms*

The reactions of Zn in the body fluid can be described as:

$$Zn \rightarrow Zn^{2+} + 2e^{-}$$

$$2H_2O + O_2 + 4e^{-} \rightarrow 4OH^{-}$$

leading to the formation of corrosion products:

$$Zn^{2+} + 2OH^{-} \rightarrow Zn(OH)_2$$

$$Zn^{2+} + 2OH^{-} \rightarrow ZnO + H_2O$$

Due to the presence of chloride ions in the body fluid, the corrosion products react with chloride ions to form soluble chloride salts:

$$6Zn(OH)_2 + Zn^{2+} + 2Cl^{-} \rightarrow 6Zn(OH)_2 \cdot ZnCl_2$$

$$4ZnO + 4H_2O + Zn^{2+} + 2Cl^{-} \rightarrow 4Zn(OH)_2 \cdot ZnCl_2$$

To reveal the static and dynamic biodegradation mechanisms of the AM porous Zn specimens, we also studied their biodegradation behavior at micro- and macro-scales. At the micro-scale, SEM, FTIR, and XPS analyses revealed the gradual formation of the biodegradation products with immersion time. At the start of the *in vitro* biodegradation tests, Zn was dissolved and $Zn(OH)_2$ formed on the surface of the specimen. As ZnO is more stable than $Zn(OH)_2$, $Zn(OH)_2$ gradually transformed into ZnO, which was confirmed by the XPS analysis, showing the gradually increasing percentages of ZnO (Fig. 5b and c). At the same time, CO_3^{2-}, P,and Ca participated in the formation of the biodegradation products, as shown by both the ICP results and EDS analysis. The concentrations of P and Ca ions in the medium gradually decreased with time (Fig. 3d and e), while the atomic percentages of P and Ca in the biodegradation products increased, as indicated by the EDS analysis (Fig. 4d–f). Similar trends were observed in the FTIR results (Fig. 4i). At the more advanced stages of biodegradation, carbonates appeared to have formed on the top of the biodegradation layer (Fig. 4g), which can also be observed in the FTIR (Fig. 4i) and XPS graphs (Fig. 5d and e). The formed protective layer enhanced the biodegradation resistance of Zn, while it was simultaneously being attacked by Cl^{-}. At the beginning, the buildup of the biodegradation layer was more dominant than the damage caused by Cl^{-}. That is why R_f, R_t, and LPR increased up to 7 days. After day 7, the dissolution of the protective layer may have caused R_f, R_t, and LPR to decrease. After day 21, R_f, R_t, and LPR increased again, probably because of the further formation of the passive layer [53]. The Bode impedance graph exhibited a similar trend of impedance variation. At the low frequency range, the impedance modulus values indicated the resistance of charge transfer and separation processes of the degrading system at the Zn surface. In the middle frequency range, the impedance modulus changes related to capacitive and resistive evolutions by formation or (partial) dissolution of the biodegradation layer on the Zn surface.

At the macro level, μCT suggested that the specimens experienced more localized biodegradation under the static condition. Moreover, localized biodegradation mainly occurred at the bottom and at the core of the specimens (Fig. 9, red square). This phenomenon was likely caused by the stagnant flow of r-SBF entrapped in the narrow gap between the specimens and the beaker. Cl^{-} became accumulated at these locations and destroyed the passive layer locally.Pitting or crevice-like corrosion would then take place. On the contrary, the dynamic flow prevented the adsorption of Cl^{-} on the surface of the corroded layer, thereby ensuring the homogeneity of the biodegradation process (Fig. 9) [60,81]. In total, larger volume of biodegradation products was formed under the dynamic biodegradation condition than the static one, indicating a faster rate of biodegradation. The ICP results also showed that the concentrations of P and Ca ions were lower under the dynamic flow condition (Fig. 3d and e). The differences between the static condition and dynamic condition in biodegradation rate and biodegradation mechanism observed at different locations within the specimens underscore the fact that, besides the selection of the biomaterial, the topological design of the porous structure is equally important in controlling the biodegradation profile of the resulting implants.

4.4. *Unique mechanical behavior*

Similar to AM porous pure Fe [38], titanium, and tantalum [11,82], the AM porous Zn specimens showed smooth stress-strain curves with no undulations at the plateau stage during the uniaxial compression tests. The curve started linearly, meaning that the porous structure was still in the elastic region. Then, the slope decreased rapidly when plastic deformation in the struts occurred, after which the plateau region appeared with almost no fluctuations. The specimens maintained their cylindrical shape at 60% strain (Fig. 8a inlay). This could be ascribed to the highly ductile behavior of pure Zn. Towards the end of the test, the slope increased significantly again, which could be attributed to the densification of the porous structure. The mechanical properties of the AM porous Zn ($E = 786$ MPa, $\sigma_y = 10.8$ MPa) stayed within the scope of the values of cancellous bone ($E = 10$ – 2000 MPa, $\sigma_y =$ 0.2 - 80 MPa [56]). As the bulk pure Zn has a tensile strength of

28–120 MPa [25], AM Zn-based alloys with good biocompatibility [83], such as Zn-Mg, Zn-Ca et al., should be developed in the future in order to improve its mechanical properties to match those of cortical bone (σ_y= 170–193 MPa [84]). Surprisingly, after *in vitro* biodegradation tests, the mechanical properties of AM porous Zn improved as compared to those of the as-built specimens. Although similar results were found at the early stages of biodegradation of AM porous Mg and Fe [37,38], the mechanical properties of biodegraded AM porous Zn were higher than those of its as-built counterpart, even after 4 weeks of *in vitro* immersion (Fig. 8b and c). Interestingly, the specimens subjected to the dynamic biodegradation condition had a higher yield strength and a higher elastic modulus, as compared to those biodegraded statically. Considering a 7.8% volume reduction of the Zn scaffold during the dynamic immersion tests for 28 days, the increases in the mechanical properties of the biodegradable metal over time could be attributed to the contributions of the biodegradation products. This explanation is supported by the hardness value of the biodegradation products which is almost 5 times as high as the hardness of the AM Zn. The AM porous Zn during biodegradation may be hypothetically regarded as a composite material consisting of a metal (Zn) substrate and a ceramic surface layer (the biodegradation products). While the progressing biodegradation deteriorated the mechanical properties of the Zn metal, the formation of the biodegradation products could help in retaining or even improving its mechanical properties. In the case of the statically tested specimens, however, smaller volume of biodegradation products was less effective in playing this role and more localized biodegradation led to decreases in yield strength. This may also explain the fluctuations of the yield strength of the statically tested specimens with time. It is however important to note that although hardness can be converted approximately to strength, the ratio varies from ductile metal to brittle ceramic over a wide range [85]. Moreover, the bonding strength between the struts and biodegradation products may also affect the mechanical properties of degraded specimens. Therefore, an in-depth study is needed to ascertain the role of the biodegradation products in compensating for the loss of the strength of the struts and the scaffold as a whole during biodegradation.

These observations, together with the absolute values of the bone-mimicking mechanical properties of AM porous Zn, suggest that AM porous Zn is a promising candidate for the design and fabrication of bone-substituting orthopedic implants. Furthermore, as the degradation products can indeed improve the mechanical properties of porous Zn, one can imagine that, with the regeneration of tissues over time, the mechanical properties can be further improved. It is then important to reconsider what should be the required mechanical properties of a biodegradable porous implant. The initial mechanical properties may not be necessarily as high as those of human bone. Of course, *in vivo* tests are still needed to further confirm the observed changes in mechanical property over time. Moreover, thorough mechanical tests, including fatigue and creep, in relation to natural aging and static recrystallization should be performed to address the mechanical compatibility issues of AM porous Zn fully [83].

4.5. In vitro *cell responses*

Using the latest modification of ISO 10,993 for evaluating the biocompatibility of medical devices, we investigated the biological safety of the biodegradable AM porous Zn [86,87]. To this end, we used direct and indirect (extraction-based) cytocompatibility testing and compared the AM Zn scaffolds with identically produced and likewise treated scaffolds of Ti-6Al-4 V - a gold standard material for orthopedic implants. Of note, we used a harsh 72 h extraction regime with the serum-containing medium that allowed for the extraction of both polar and non-polar substances (ISO10993-5, 2009) [87,88] in a physiological cell culture environment (*i.e.*, 37 °C, pH 7.2–7.4, 5% CO_2). *In vivo*, vascularization ensures, among others, waste product removal. In agreement with ISO 10,993, modified for bioabsorbable biomaterials, we used diluted (*i.e.*, 10X) Zn extracts, which is further in line with previous reports recommending to use 9X to 14X diluted extracts from biodegradable metals, such as Mg alloys [87]. Using 10X diluted extracts was also reported earlier in the cases of AM porous Mg and Fe [37,38]. We further used MTS assays as the most accepted *in vitro* evaluation for extract-based cytotoxicity screening [87]. Until 48 h, the cytotoxicity profiles of Zn extracts were not significantly different from those derived from identically designed Ti-6Al-4 V specimens. Even in the extended incubations up to 72 h, which is the longest recommended period by ISO 10,993 [89], the Zn extracts were well tolerated by osteoblast-like cells, showing compromised metabolic activity only in about 15% of the cell population and demonstrating a concentration-dependent effect, which is consistent with the findings of other researchers [90]. The majority of the currently available studies report good cell viability of diluted Zn extracts [63,91,92]. However, a few studies have recently reported good cytocompatibility of even undiluted extracts [93,94]. The desirable cytocompatibility of Zn may be attributed to its low biodegradation rate in plasma and less severe changes in the local pH [27,65].

In addition to indirectly evaluating the cytocompatibility of the AM porous Zn specimens, we investigated the cell viability directly on the Zn scaffolds through fluorescent live/dead imaging. While this approach is semi-quantitative, it enabled us to study the cell morphology on the scaffolds, and cell distribution within the scaffolds. From peripheral scanning and cross-sectional imaging of the scaffolds, MG-63 cells appeared to be evenly distributed around and within the scaffolds. The majority of cells was further viable and appeared to be intimately attached to the Zn scaffold surface, already after 24 h of seeding. Cell morphologies on Zn were similar to those on Ti-6Al-4V: cells covered all surfaces of the specimens. This is in agreement with earlier studies showing that Zn-based biomaterials supported cell adhesion, viability, and proliferation [95]. Interestingly, several studies have recently reported that Zn ions can enhance gene expression, cell survival and growth, as well as the differentiation of progenitor cells [96–98]. At low concentrations, Zn^{2+} has been furthermore reported to have a positive effect on the cellular activity of human vascular cells [99,100]. Although Zn is also reported to be involved in modulating pro-inflammatory responses, it is actually crucial for sustaining a proper immune function, too [101]. AM porous Zn implants, therefore, holds a lot of potential for orthopedic applications, as their biodegradation products may facilitate vascularization and, thus, bone regeneration.

5. Conclusions

AM topologically ordered biodegradable porous Zn showed potential to fulfill the multiple requirements for an ideal bone-substituting biomaterial. First, the mechanical properties of the as-built AM porous Zn (E = 786 MPa, σ_y= 10.8 MPa) are within the scope reported for cancellous bone and thus are high enough to provide adequate mechanical support. After 4 weeks of *in vitro* immersion, the mechanical properties of the AM porous Zn even increased (E = 879 MPa, σ_y= 12.0 MPa). Secondly, the fabricated scaffolds presented a precise topology and completely interconnected pores, as designed. Thirdly, the biodegradation rate of the AM porous Zn was moderate with ≈7.8% and ≈3.6% volume losses after 4 weeks of dynamic and static *in vitro* immersion, respectively. Moreover, the AM porous Zn exhibited good biocompatibility *in vitro*. Therefore, with the proper scaffold design and

alloying, Zn-based biomaterials will hold great potential to become one group of the next-generation functional biodegradable biomaterials for orthopedic applications and to provide long-awaited solutions to the treatment of large bony defects.

Declaration of Competing Interest

The authors declare that they have no known competing financial interests or personal relationships that could have appeared to influence the work reported in this paper.

Acknowledgments

The research reported in this paper was financially supported by the Prosperos project, funded by the Interreg VA Flanders – The Netherlands program, CCI Grant No. 2014TC16RFCB04. Y.L. thanks the China Scholarship Council (CSC) for financial support. K.L. thanks VLAIO (Flanders Agency for Innovation and Entrepreneurship) for the financial support (IWT140257). Richard Huizenga at the Department of Materials Science and Engineering, Delft University of Technology, is acknowledged for the XRD analysis.

Supplementary material

Supplementary material associated with this article can be found, in the online version, at doi:10.1016/j.actbio.2019.10.034.

References

[1] A.A. Zadpoor, J. Malda, Additive manufacturing of biomaterials, iissues, and organs, Ann. Biomed. Eng. 45 (2017) 1–11.
[2] L. Murr, S. Gaytan, F. Medina, H. Lopez, E. Martinez, B. Machado, D. Hernandez, L. Martinez, M. Lopez, R. Wicker, Next-generation biomedical implants using additive manufacturing of complex, cellular and functional mesh arrays, Philos. Trans. R. Soc. A. 368 (2010) 1999–2032.
[3] A.A. Zadpoor, Mechanical performance of additively manufactured meta-biomaterials, Acta Biomater. 85 (2019) 41–59.
[4] X. Wang, S. Xu, S. Zhou, W. Xu, M. Leary, P. Choong, M. Qian, M. Brandt, Y.M. Xie, Topological design and additive manufacturing of porous metals for bone scaffolds and orthopaedic implants: a review, Biomaterials 83 (2016) 127–141.
[5] A.A. Zadpoor, Mechanics of additively manufactured biomaterials, J. Mech. Behav. Biomed. Mater. 70 (2017) 1–6.
[6] A.A. Zadpoor, Current trends in metallic orthopedic biomaterials: from additive manufacturing to bio-functionalization, infection prevention, and beyond, Int. J. Mol. Sci. 19 (2018) 2684.
[7] A.H. Yusop, A.A. Bakir, N.A. Shaharom, M.R. Abdul Kadir, H. Hermawan, Porous biodegradable metals for hard tissue scaffolds: a review, Int. J. Biomater. 2012 (2012) 10.
[8] C. Yan, L. Hao, A. Hussein, P. Young, D. Raymont, Advanced lightweight 316L stainless steel cellular lattice structures fabricated via selective laser melting, Mater Des. 55 (2014) 533–541.
[9] S.M. Ahmadi, R. Hedayati, Y. Li, K. Lietaert, N. Tümer, A. Fatemi, C.D. Rans, B. Pouran, H. Weinans, A.A. Zadpoor, Fatigue performance of additively manufactured meta-biomaterials: the effects of topology and material type, Acta Biomater. 65 (2018) 292–304.
[10] S.M. Ahmadi, R. Kumar, E.V. Borisov, R. Petrov, S. Leeflang, Y. Li, N. Tümer, R. Huizenga, C. Ayas, A.A. Zadpoor, V.A. Popovich, From microstructural design to surface engineering: a tailored approach for improving fatigue life of additively manufactured meta-biomaterials, Acta Biomater. 83 (2019) 153–166.
[11] R. Wauthle, J. van der Stok, S. Amin Yavari, J. Van Humbeeck, J.-P. Kruth, A.A. Zadpoor, H. Weinans, M. Mulier, J. Schrooten, Additively manufactured porous tantalum implants, Acta Biomater. 14 (2015) 217–225.
[12] R. Hedayati, S.M. Ahmadi, K. Lietaert, B. Pouran, Y. Li, H. Weinans, C.D. Rans, A.A. Zadpoor, Isolated and modulated effects of topology and material type on the mechanical properties of additively manufactured porous biomaterials, J. Mech. Behav. Biomed. Mater. 79 (2018) 254–263.
[13] M. Moravej, D. Mantovani, Biodegradable metals for cardiovascular stent application: interests and new opportunities, Int. J. Mol. Sci. 12 (2011) 4250.
[14] A.A. Zadpoor, Additively manufactured porous metallic biomaterials, J. Mater Chem. B. (2019).
[15] Y.Liu, Y.Zheng, X.-.H.Chen, J.-.A.Yang, H.Pan, D.Chen, L.Wang, J.Zhang, D.Zhu, S.Wu, K.W.K.Yeung, R.-.C.Zeng, Y.Han, S.Guan. Fundamental theory of biodegradable metals—definition, criteria, and design. Adv. Funct. Mater. 0:1805402.
[16] H. Hermawan, Updates on the research and development of absorbable metals for biomedical applications, Prog. Biomater. 7 (2018) 93–110.
[17] Y.F. Zheng, X.N. Gu, F. Witte, Biodegradable metals, Mater Sci. Eng. R Rep. 77 (2014) 1–34.
[18] Q. Peng, Y. Huang, L. Zhou, N. Hort, K.U. Kainer, Preparation and properties of high purity Mg–y biomaterials, Biomaterials 31 (2010) 398–403.
[19] D. Zhao, F. Witte, F. Lu, J. Wang, J. Li, L. Qin, Current status on clinical applications of magnesium-based orthopaedic implants: a review from clinical translational perspective, Biomaterials 112 (2017) 287–302.
[20] T. Kraus, F. Moszner, S. Fischerauer, M. Fiedler, E. Martinelli, J. Eichler, F. Witte, E. Willbold, M. Schinhammer, M. Meischel, P.J. Uggowitzer, J.F. Löffler, A. Weinberg, Biodegradable fe-based alloys for use in osteosynthesis: outcome of an *in vivo* study after 52weeks, Acta Biomater. 10 (2014) 3346–3353.
[21] D. Pierson, J. Edick, A. Tauscher, E. Pokorney, P. Bowen, J. Gelbaugh, J. Stinson, H. Getty, C.H. Lee, J. Drelich, J. Goldman, A simplified *in vivo* approach for evaluating the bioabsorbable behavior of candidate stent materials, J. Biomed. Mater Res. B Appl. Biomater. 100B (2012) 58–67.
[22] D. Andreas, H. Thomas, B.F. Wilhelm, P. Matthias, *In vitro* and *in vivo* corrosion properties of new iron–manganese alloys designed for cardiovascular applications, J. Biomed. Mater Res. B Appl. Biomater. 103 (2015) 649–660.
[23] L.-.Y. Li, L.-.Y. Cui, R.-.C. Zeng, S.-.Q. Li, X.-.B. Chen, Y. Zheng, M.B. Kannan, Advances in functionalized polymer coatings on biodegradable magnesium alloys – A review, Acta Biomater. 79 (2018) 23–36.
[24] Y. Zheng, X. Xu, Z. Xu, J. Wang, H. Cai, Development of fe-based degradable metallic biomaterials, Metallic Biomater: Wiley-VCH Verlag GmbH Co. KGaA (2017) 113–160.
[25] J. Venezuela, M.S. Dargusch, The influence of alloying and fabrication techniques on the mechanical properties, biodegradability and biocompatibility of zinc: a comprehensive review, Acta Biomater. 87 (2019) 1–40.
[26] G. Katarivas Levy, J. Goldman, E. Aghion, The prospects of zinc as a structural material for biodegradable implants—a review paper, Metals (Basel) 7 (2017) 402.
[27] D. Zhu, I. Cockerill, Y. Su, Z. Zhang, J. Fu, K.-.W. Lee, J. Ma, C. Okpokwasili, L. Tang, Y. Zheng, Y.-.X. Qin, Y. Wang, Mechanical strength, biodegradation, and *in vitro* and *in vivo* biocompatibility of Zn biomaterials, ACS Appl. Mater Interf. (2019).
[28] K. Falchuk, The biochemical basis of zinc physiology, Physiol. Rev. 73 (1993) 79–118.
[29] C.J. Frederickson, J.-.Y. Koh, A.I. Bush, The neurobiology of zinc in health and disease, Nat. Rev. Neurosci. 6 (2005) 449–462.
[30] X. Liu, J. Sun, K. Qiu, Y. Yang, Z. Pu, L. Li, Y. Zheng, Effects of alloying elements (Ca and Sr) on microstructure, mechanical property and *in vitro* corrosion behavior of biodegradable Zn–1.5Mg alloy, J. Alloys Compd. 664 (2016) 444–452.
[31] P.K. Bowen, J. Drelich, J. Goldman, Zinc exhibits ideal physiological corrosion behavior for bioabsorbable stents, Adv. Mater. 25 (2013) 2577–2582.
[32] L. Zhao, Z. Zhang, Y. Song, S. Liu, Y. Qi, X. Wang, Q. Wang, C. Cui, Mechanical properties and *in vitro* biodegradation of newly developed porous zn scaffolds for biomedical applications, Mater Des. 108 (2016) 136–144.
[33] J. Niu, Z. Tang, H. Huang, J. Pei, H. Zhang, G. Yuan, W. Ding, Research on a Zn-Cu alloy as a biodegradable material for potential vascular stents application, Mater Sci. Eng. C. 69 (2016) 407–413.
[34] X. Gu, Y. Zheng, Y. Cheng, S. Zhong, T. Xi, *In vitro* corrosion and biocompatibility of binary magnesium alloys, Biomaterials 30 (2009) 484–498.
[35] Y. Qin, P. Wen, H. Guo, D. Xia, Y. Zheng, L. Jauer, R. Poprawe, M. Voshage, J.H. Schleifenbaum, Additive manufacturing of biodegradable metals: current research status and future perspectives, Acta Biomater. (2019).
[36] J.P. Kruth, L. Froyen, J. Van Vaerenbergh, P. Mercelis, M. Rombouts, B. Lauwers, Selective laser melting of iron-based powder, J. Mater Process Technol. 149 (2004) 616–622.
[37] Y. Li, J. Zhou, P. Pavanram, M.A. Leeflang, L.I. Fockaert, B. Pouran, N. Tümer, K.U. Schröder, J.M.C. Mol, H. Weinans, H. Jahr, A.A. Zadpoor, Additively manufactured biodegradable porous magnesium, Acta Biomater. 67 (2018) 378–392.
[38] Y. Li, H. Jahr, K. Lietaert, P. Pavanram, A. Yilmaz, L.I. Fockaert, M.A. Leeflang, B. Pouran, Y. Gonzalez-Garcia, H. Weinans, J.M.C. Mol, J. Zhou, A.A. Zadpoor, Additively manufactured biodegradable porous iron, Acta Biomater. 77 (2018) 380–393.
[39] P. Wen, Y. Qin, Y. Chen, M. Voshage, L. Jauer, R. Poprawe, J. Henrich Schleifenbaum, Laser additive manufacturing of Zn porous scaffolds: shielding gas flow, surface quality and densification, J. Mater Sci. Technol. (2018).
[40] D. Carluccio, A.G. Demir, L. Caprio, B. Previtali, M.J. Bermingham, M.S. Dargusch, The influence of laser processing parameters on the densification and surface morphology of pure Fe and Fe-35mn scaffolds produced by selective laser melting, J. Manuf. Process. 40 (2019) 113–121.
[41] Y. Li, H. Jahr, X.Y. Zhang, M.A. Leeflang, W. Li, B. Pouran, F.D. Tichelaar, H. Weinans, J. Zhou, A.A. Zadpoor, Biodegradation-affected fatigue behavior of additively manufactured porous magnesium, Addit Manuf. 28 (2019) 299–311.
[42] Y. Li, K. Lietaert, W. Li, X.Y. Zhang, M.A. Leeflang, J. Zhou, A.A. Zadpoor, Corrosion fatigue behavior of additively manufactured biodegradable porous iron, Corros Sci. 156 (2019) 106–116.
[43] K. Lietaert, B. Neirinck, J. Plas, J. Vleugels, Influence of unit cell architecture and of relative density on the mechanical properties of additively manufactured zn scaffolds as biodegradable implant materials, in: Proceedings of the Euro PM International Powder Metallurgy Congress and Exhibition. Politecnico di Milano, The European Powder Metallurgy Association, Italy, 2017, pp. 1–7.

[44] Y. Qin, P. Wen, M. Voshage, Y. Chen, P.G. Schückler, L. Jauer, D. Xia, H. Guo, Y. Zheng, J.H. Schleifenbaum, Additive manufacturing of biodegradable zn-xwe43 porous scaffolds: formation quality, microstructure and mechanical properties, Mater Des. 181 (2019) 107937.
[45] K. Lietaert, W. Baekelant, L. Thijs, J. Vleugels, Direct metal printing of zinc: from single laser tracks to high density parts, in: Proceedings of the European Congress and Exhibition on Powder Metallurgy. European PM Conference Swerea KIMAB, The European Powder Metallurgy Association, Sweden, 2016, pp. 1–6.
[46] A. Oyane, H.-.M. Kim, T. Furuya, T. Kokubo, T. Miyazaki, T. Nakamura, Preparation and assessment of revised simulated body fluids, J. Biomed. Mater Res. A. 65A (2003) 188–195.
[47] F. Zhao, B. van Rietbergen, K. Ito, S. Hofmann, Flow rates in perfusion bioreactors to maximise mineralisation in bone tissue engineering *in vitro*, J. Biomech. 79 (2018) 232–237.
[48] M.E. Gomes, V.I. Sikavitsas, E. Behravesh, R.L. Reis, A.G. Mikos, Effect of flow perfusion on the osteogenic differentiation of bone marrow stromal cells cultured on starch-based three-dimensional scaffolds, J. Biomed. Mater Res. A. 67A (2003) 87–95.
[49] J.R. Vetsch, D.C. Betts, R. Müller, S. Hofmann, Flow velocity-driven differentiation of human mesenchymal stromal cells in silk fibroin scaffolds: A combined experimental and computational approach, PLoS One 12 (2017) e0180781.
[50] Y. Xin, K. Huo, H. Tao, G. Tang, P.K. Chu, Influence of aggressive ions on the degradation behavior of biomedical magnesium alloy in physiological environment, Acta Biomater. 4 (2008) 2008–2015.
[51] Y. Chen, S. Zhao, B. Liu, M. Chen, J. Mao, H. He, Y. Zhao, N. Huang, G. Wan, Corrosion-Controlling and osteo-compatiblemgion-integratedphyticacid (Mg-PA) coating on magnesiumsubstrate for biodegradable implants application, ACS Appl. Mater Interfaces 6 (2014) 19531–19543.
[52] Y. Sheng, H. Zhou, Z. Li, L. Chen, X. Wang, X. Zhao, L. Wei, Improved blood compatibility and cyto-compatibility of Zn-1Mg via plasma electrolytic oxidation, Materialia 5 (2019) 100244.
[53] L. Liu, Y. Meng, A.A. Volinsky, H.-J. Zhang, L.-.N. Wang, Influences of albumin on *in vitro* corrosion of pure Zn in artificial plasma, Corros. Sci. 153 (2019) 341–356.
[54] X. Liu, H. Yang, Y. Liu, P. Xiong, H. Guo, H.-.H. Huang, Y. Zheng, Comparative studies on degradation behavior of pure zinc in various simulated body fluids, JOM 71 (2019) 1414–1425.
[55] S. Champagne, E. Mostaed, F. Safizadeh, E. Ghali, M. Vedani, H. Hermawan, *In vitro* degradation of absorbable zinc alloys in artificial urine, Materials (Basel) 12 (2019) 295.
[56] M. Yazdimamaghani, M. Razavi, D. Vashaee, K. Moharamzadeh, A.R. Boccaccini, L. Tayebi, Porous magnesium-based scaffolds for tissue engineering, Mater Sci. Eng. C. 71 (2017) 1253–1266.
[57] L.-.E. Loh, C.-.K. Chua, W.-.Y. Yeong, J. Song, M. Mapar, S.-.L. Sing, Z.-.H. Liu, D.-.Q. Zhang, Numerical investigation and an effective modelling on the selectivelasermelting (SLM) process with aluminium alloy 6061, Int. J. Heat Mass Trans. 80 (2015) 288–300.
[58] P. Wen, M. Voshage, L. Jauer, Y. Chen, Y. Qin, R. Poprawe, J.H. Schleifenbaum, Laser additive manufacturing of Zn metal parts for biodegradable applications: processing, formation quality and mechanical properties, Mater Des. 155 (2018) 36–45.
[59] T. DebRoy, H.L. Wei, J.S. Zuback, T. Mukherjee, J.W. Elmer, J.O. Milewski, A.M. Beese, A. Wilson-Heid, A. De, W. Zhang, Additive manufacturing of metallic components – Process, structure and properties, Prog. Mater Sci. 92 (2018) 112–224.
[60] J. Lévesque, H. Hermawan, D. Dubé, D. Mantovani, Design of a pseudo-physiological test bench specific to the development of biodegradable metallic biomaterials, Acta Biomater. 4 (2008) 284–295.
[61] N.T. Kirkland, N. Birbilis, M.P. Staiger, Assessing the corrosion of biodegradable magnesium implants: a critical review of current methodologies and their limitations, Acta Biomater. 8 (2012) 925–936.
[62] L. Liu, Y. Meng, C. Dong, Y. Yan, A.A. Volinsky, L.-.N. Wang, Initial formation of corrosion products on pure zinc in simulated body fluid, J. Mater Sci. Technol. 34 (2018) 2271–2282.
[63] C. Shen, X. Liu, B. Fan, P. Lan, F. Zhou, X. Li, H. Wang, X. Xiao, L. Li, S. Zhao, Z. Guo, Z. Pu, Y. Zheng, Mechanical properties, *in vitro* degradation behavior, hemocompatibility and cytotoxicity evaluation of Zn–1.2Mg alloy for biodegradable implants, RSC Adv. 6 (2016) 86410–86419.
[64] H.F. Li, X.H. Xie, Y.F. Zheng, Y. Cong, F.Y. Zhou, K.J. Qiu, X. Wang, S.H. Chen, L. Huang, L. Tian, L. Qin, Development of biodegradable zn-1x binary alloys with nutrient alloying elements mg, Ca Sr. Sci. Rep. 5 (2015) 10719.
[65] K. Törne, M. Larsson, A. Norlin, J. Weissenrieder, Degradation of zinc in saline solutions, plasma, and whole blood, J. Biomed. Mater Res. B Appl. Biomater. 104 (2016) 1141–1151.
[66] P. Sotoudeh Bagha, S. Khaleghpanah, S. Sheibani, M. Khakbiz, A. Zakeri, Characterization of nanostructured biodegradable Zn-Mn alloy synthesized by mechanical alloying, J Alloys Compd. 735 (2018) 1319–1327.
[67] X. Liu, J. Sun, F. Zhou, Y. Yang, R. Chang, K. Qiu, Z. Pu, L. Li, Y. Zheng, Micro-alloying with mn in Zn–Mg alloy for future biodegradable metals application, Mater Des. 94 (2016) 95–104.
[68] S. Zhao, C.T. McNamara, P.K. Bowen, N. Verhun, J.P. Braykovich, J. Goldman, J.W. Drelich, Structural characteristics and *in vitro* biodegradation of a novel Zn-Li alloy prepared by induction melting and hot rolling, Metall. Mater Trans. A. 48 (2017) 1204–1215.
[69] J. Cheng, B. Liu, Y.H. Wu, Y.F. Zheng, Comparative *in vitro* study on pure metals (Fe, Mn,Mg,Zn and W) as biodegradable metals, J. Mater Sci. Technol. 29 (2013) 619–627.
[70] E. Mostaed, M. Sikora-Jasinska, A. Mostaed, S. Loffredo, A.G. Demir, B. Previtali, D. Mantovani, R. Beanland, M. Vedani, Novel zn-based alloys for biodegradable stent applications: design, development and *in vitro* degradation, J. Mech. Behav. Biomed. Mater. 60 (2016) 581–602.
[71] Y. Yang, F. Yuan, C. Gao, P. Feng, L. Xue, S. He, C. Shuai, A combined strategy to enhance the properties of Zn by laser rapid solidification and laser alloying, J. Mech. Behav. Biomed. Mater. 82 (2018) 51–60.
[72] D. Vojtěch, J. Kubásek, J. Šerák, P. Novák, Mechanical and corrosion properties of newly developed biodegradable Zn-based alloys for bone fixation, Acta Biomater. 7 (2011) 3515–3522.
[73] Z. Tang, J. Niu, H. Huang, H. Zhang, J. Pei, J. Ou, G. Yuan, Potential biodegradable Zn-Cu binary alloys developed for cardiovascular implant applications, J. Mech. Behav. Biomed. Mater. 72 (2017) 182–191.
[74] M. Sikora-Jasinska, E. Mostaed, A. Mostaed, R. Beanland, D. Mantovani, M. Vedani, Fabrication, mechanical properties and *in vitro* degradation behavior of newly developed Znag alloys for degradable implant applications, Mater Sci. Eng., C. 77 (2017) 1170–1181.
[75] A. Kafri, S. Ovadia, G. Yosafovich-Doitch, E. Aghion, *In vivo* performances of pure Zn and Zn–Fe alloy as biodegradable implants, J. Mater Sci. Mater Med. 29 (2018) 94.
[76] H. Yang, C. Wang, C. Liu, H. Chen, Y. Wu, J. Han, Z. Jia, W. Lin, D. Zhang, W. Li, W. Yuan, H. Guo, H. Li, G. Yang, D. Kong, D. Zhu, K. Takashima, L. Ruan, J. Nie, X. Li, Y. Zheng, Evolution of the degradation mechanism of pure zinc stent in the one-year study of rabbit abdominal aorta model, Biomaterials 145 (2017) 92–105.
[77] A.J. Drelich, S. Zhao, R.J. Guillory, J.W. Drelich, J. Goldman, Long-term surveillance of zinc implant in murine artery: surprisingly steady biocorrosion rate, Acta Biomater. 58 (2017) 539–549.
[78] P.K. Bowen, R.J. Guillory, E.R. Shearier, J.-.M. Seitz, J. Drelich, M. Bocks, F. Zhao, J. Goldman, Metallic zinc exhibits optimal biocompatibility for bioabsorbable endovascular stents, Mater Sci. Eng. C. 56 (2015) 467–472.
[79] S. Zhao, J.-.M. Seitz, R. Eifler, H.J. Maier, R.J. Guillory, E.J. Earley, A. Drelich, J. Goldman, J.W. Drelich, Zn-Li alloy after extrusion and drawing: structural, mechanical characterization, and biodegradation in abdominal aorta of rat, Mater Sci. Eng. C. 76 (2017) 301–312.
[80] S.A. Arab, G.R. J. II, S. Daniel, G. Jeremy, D.J. W., Effect of plla coating on corrosion and biocompatibility of zinc in vascular environment, Surf Innov. 5 (2017) 211–220.
[81] Y. Zong, G. Yuan, X. Zhang, L. Mao, J. Niu, W. Ding, Comparison of biodegradable behaviors of AZ31 and Mg–Nd–Zn–Zr alloys in hank's physiological solution, Mater Sci. Eng. B. 177 (2012) 395–401.
[82] R. Wauthle, S.M. Ahmadi, S. Amin Yavari, M. Mulier, A.A. Zadpoor, H. Weinans, J. Van Humbeeck, J.-.P. Kruth, J. Schrooten, Revival of pure titanium for dynamically loaded porous implants using additive manufacturing, Mater Sci. Eng. C. 54 (2015) 94–100.
[83] G. Li, H. Yang, Y. Zheng, X.-.H. Chen, J.-.A. Yang, D. Zhu, L. Ruan, K. Takashima, Challenges in the use of zinc and its alloys as biodegradable metals: perspective from biomechanical compatibility, Acta Biomater. (2019).
[84] S. Wu, X. Liu, K.W.K. Yeung, C. Liu, X. Yang, Biomimetic porous scaffolds for bone tissue engineering, Mater Sci. Eng. R Rep. 80 (2014) 1–36.
[85] P. Zhang, S.X. Li, Z.F. Zhang, General relationship between strength and hardness, Mater Sci. Eng. A. 529 (2011) 62–73.
[86] H.-.S. Han, H.-.K. Kim, Y.-.C. Kim, H.-.K. Seok, Y.-.Y. Kim, Conventional and improved cytotoxicity test methods of newly developed biodegradable magnesium alloys, Met Mater Int. 21 (2015) 1108–1117.
[87] J. Wang, F. Witte, T. Xi, Y. Zheng, K. Yang, Y. Yang, D. Zhao, J. Meng, Y. Li, W. Li, K. Chan, L. Qin, Recommendation for modifying current cytotoxicity testing standards for biodegradable magnesium-based materials, Acta Biomater. 21 (2015) 237–249.
[88] Y. Su, I. Cockerill, Y. Wang, Y.-.X. Qin, L. Chang, Y. Zheng, D. Zhu, Zinc-based biomaterials for regeneration and therapy, Trends Biotechnol. 37 (2019) 428–441.
[89] J. Fischer, M.H. Prosenc, M. Wolff, N. Hort, R. Willumeit, F. Feyerabend, Interference of magnesium corrosion with tetrazolium-based cytotoxicity assays, Acta Biomater. 6 (2010) 1813–1823.
[90] P. Li, C. Schille, E. Schweizer, F. Rupp, A. Heiss, C. Legner, U.E. Klotz, J. Geis-Gerstorfer, L. Scheideler, Mechanical characteristics, *in vitro* degradation, cytotoxicity, and antibacterial evaluation of Zn-4.0Ag alloy as a biodegradable material, Int. J. Mol. Sci. 19 (2018) 755.
[91] J. Kubásek, D. Vojtěch, E. Jablonská, I. Pospíšilová, J. Lipov, T. Ruml, Structure, mechanical characteristics and *in vitro* degradation, cytotoxicity, genotoxicity and mutagenicity of novel biodegradable Zn–Mg alloys, Mater Sci Eng, C. 58 (2016) 24–35.
[92] C. Shuai, Y. Cheng, Y. Yang, S. Peng, W. Yang, F. Qi, Laser additive manufacturing of zn-2al part for bone repair: formability, microstructure and properties, J. Alloys Compd. 798 (2019) 606–615.
[93] H. Li, H. Yang, Y. Zheng, F. Zhou, K. Qiu, X. Wang, Design and characterizations of novel biodegradable ternary zn-based alloys with iia nutrient alloying elements mg, Ca Sr. Mater Des. 83 (2015) 95–102.
[94] H.R. Bakhsheshi-Rad, E. Hamzah, H.T. Low, M. Kasiri-Asgarani, S. Farahany, E. Akbari, M.H. Cho, Fabrication of biodegradable Zn-Al-Mg alloy: mechanical properties, corrosion behavior, cytotoxicity and antibacterial activities, Mater Sci. Eng. C. 73 (2017) 215–219.

[95] D. Zhu, Y. Su, M.L. Young, J. Ma, Y. Zheng, L. Tang, Biological responses and mechanisms of human bone marrow mesenchy malstemcells to Zn and Mg biomaterials, ACS Appl. Mater Interf. 9 (2017) 27453–27461.
[96] Y. Qiao, W. Zhang, P. Tian, F. Meng, H. Zhu, X. Jiang, X. Liu, P.K. Chu, Stimulation of bone growth following zinc incorporation into biomaterials, Biomaterials 35 (2014) 6882–6897.
[97] J. Yu, L. Xu, K. Li, N. Xie, Y. Xi, Y. Wang, X. Zheng, X. Chen, M. Wang, X. Ye, Zinc-modified calcium silicate coatings promoteoste ogenic differentiation through TGF-β/Smad pathway and osseointegration in osteopenicrabbits, Sci. Rep. 7 (2017) 3440.
[98] G. Cama, S. Nkhwa, B. Gharibi, A. Lagazzo, R. Cabella, C. Carbone, P. Dubruel, H. Haugen, L. Di Silvio, S. Deb, The role of new zinc incorporated monetite cements on osteogenic differentiation of human mesenchymal stem cells, Mater Sci. Eng. C. 78 (2017) 485–494.
[99] J. Ma, N. Zhao, D. Zhu, Endothelial cellular responses to biodegradable metal zinc, ACS Biomater. Sci. Eng. 1 (2015) 1174–1182.
[100] E.R. Shearier, P.K. Bowen, W. He, A. Drelich, J. Drelich, J. Goldman, F. Zhao, *In vitro* cytotoxicity, adhesion, and proliferation of human vascular cells exposed to zinc, ACS Biomater Sci. Eng. 2 (2016) 634–642.
[101] N.Z. Gammoh, L. Rink, Zinc in infection and inflammation, Nutrients 9 (2017) 624.